ABSTRACT

LEITE DE MORAES, EDUARDO MALVEZZI. Harnessing High Speed Flow: Dynamic Models for Air Jet Spinning and Bladeless Turbines. (Under the direction of Dr. James Braun).

High speed flow interactions with rotating bodies play an important role in many applications. This thesis explores two areas in this field, dynamic modeling of fibers in air jet spinning, and the performance predictions of bladeless turbines.

In air jet spinning, individual fibers are twisted and wrapped to form yarn using high speed airflow. This work presents CFD studies of the flow field inside an air jet spinning chamber, coupled with dynamic models for wrap fiber motion. A geometric model based on a completed yarn, a one-dimensional equilibrium model, and a two-dimensional time dependent model were created to predict wrap velocities, combining flow field characteristics to yarn production rates. Experiments using high speed imaging were conducted to validate these models, closing the cycle from simulation to reality.

The bladeless turbine is an emerging concept that uses unique characteristics of supersonic flow to generate torque. Computational simulations were performed to assess the performance of both cylindrical and conical bladeless turbines. The analysis of results includes visualization of shock wave formation, pressure distributions, and power extraction as a function of rotational velocity. Numerical analysis and analytical equations were used to guide the geometry of a turbine suitable for testing in a laboratory environment. Modifications and analysis techniques were proposed to enable real-world testing, including the conical design which simplifies experimental integration.

By developing predictive models, this research advances the understanding of fluid-solid interactions in high speed flows, with direct applications to fiber processing and energy generation.

© Copyright 2025 by Eduardo Malvezzi Leite de Moraes

All Rights Reserved

Harnessing High Speed Flow: Dynamic Models for Air Jet Spinning and Bladeless Turbines

by
Eduardo Malvezzi Leite de Moraes

A thesis submitted to the Graduate Faculty of
North Carolina State University
in partial fulfillment of the
requirements for the degree of
Master of Science

Aerospace Engineering

Raleigh, North Carolina
2025

APPROVED BY:

Dr. James Braun
Committee Chair

Dr. Hooman Tafreshi

Dr. Venkat Narayanaswamy

BIOGRAPHY

Eduardo Malvezzi Leite de Moraes was born on November 17, 2000 in Toronto, Canada. Growing up, he had a passion for all things mechanical, electrical, and aerospace, and dreamt of becoming an engineer before he knew what the word meant. He attended Carleton University in Ottawa, Canada to pursue Aerospace Engineering. From 2021 - 2022, Eduardo worked for the National Research Council of Canada where his passion for research solidified before returning to Carleton to finish his degree, graduating in 2023 with high distinction. Eduardo joined North Carolina State University later that year to pursue a masters in aerospace engineering, and is considering pursuing a PhD. In the future, he hopes to work as an aircraft test engineer, with particular interest in the areas of propulsion and system integration. In his free time, Eduardo works on various personal projects, usually including electronics, fabrication, or radio-control models.

ACKNOWLEDGMENTS

First and foremost, I am deeply grateful to my parents and family for their unwavering support and encouragement as I pursue my dreams. Their guidance and belief in me have shaped my journey, inspiring me to reach for goals I once thought unattainable.

I extend my sincere appreciation to my advisor, Dr. James Braun, for his guidance and mentorship during my time at North Carolina State University. Being welcomed into the BEFAST Lab was a pivotal moment in my graduate studies, and I will always cherish the opportunities and experience it provided.

Finally, I would like to thank my friends – both within the lab and beyond – for their constant support, camaraderie and encouragement. Their presence has made this journey all the more meaningful.

TABLE OF CONTENTS

LIST OF TABLES

LIST OF FIGURES

1 Introduction

1.1 Fluid-Solid Interactions in High Speed Flow

High speed flow past immersed bodies plays a crucial role in many applications. Despite this, accurately predicting body behavior and optimizing the benefits of these interactions remains challenging.

Supersonic flow occurs when gaseous media travels at a rate greater than the local speed of sound, with the ratio of the flow velocity to the local speed of sound being known as the Mach number. The local speed of sound a can be derived using the continuity of mass, momentum, and energy, with a detailed derivation being presented by White [1]. Doing so results in the following equation, with γ representing the dimensionless ratio of specific heats of the gas, R representing the specific gas constant in units of $\frac{[L]^2}{[T]^2[\Theta]}$, and T representing the static temperature in absolute units.

$$a = \sqrt{\gamma R T}$$

In equation form, the Mach number is expressed as follows:

$$\mathrm{Ma} = \frac{c}{a} = \frac{c}{\sqrt{\gamma R T}}$$

Supersonic flow presents itself when the static pressure to total pressure ratio exceeds a certain critical value. This pressure ratio can be defined using isentropic relations, which also serve to define other important ratios including temperature and density. Viscous forces and inviscid, or pressure forces arising from supersonic flow can be used to perform useful work, with two applications being investigated in this thesis.

Spinning is the process of twisting and wrapping short segments of individual fibers, known as staple fibers, to form a cohesive yarn. By doing so, the tensile strength of the individual fibers can be utilized to form a continuous length of yarn. The other type of yarn commonly found is filament based, which uses continuous filaments spun together to form a yarn. Spinning continuous filaments into a cohesive yarn has several advantages over using the filament without processing. For example, blending of materials can be done more easily, and the process allows for greater control over important parameters such as yarn diameter and texture. Staple fibers include most natural fibers such as cotton, wool and hemp, with the notable exception of silk, which is a continuous fiber. Other examples of continuous fibers include synthetic fibers such as polyester, polyamide and acrylic. Continuous fibers can be cut to form staple fibers.

Numerous types of spinning machines exist, each with their own advantages and disadvantages. The most common types include ring spinning, rotor spinning, and air jet spinning. Air jet spinning was popularized in the 1980s due to its high production rates, making it an economical choice for yarn manufacturers [2]. In addition to this, air jet spinning produces less hairy yarn, which makes woven textiles more resistant to pilling [3], and simplifies the production process, eliminating the need for several pre-production steps such as roving [4].

The bladeless wavy axial turbine is a concept initially proposed by Braun et. al. in 2020 [5]. As opposed to traditional bladed turbines, the bladeless turbine uses its helical surface features to induce shock waves and expansion fans in supersonic flow. The shock waves generate a pressure differential across them, which when coupled with the surface geometry of the bladeless turbine, generates torque. Advantages of this turbine include the flexibility to operate across a wide supersonic regime, from Mach 1.2 to upwards of Mach 5, and a simplified geometry that facilitates manufacturing.

This thesis documents the work done to create new models to couple computational fluid dynamics (CFD) results to air jet spun yarn production rates, and investigates the modifications necessary to test the bladeless turbine in a university laboratory setting.

1.2 Literature Review

1.2.1 Air Jet Spinning

The field of textile technology is constantly evolving, with developments focusing on production rates and fiber modeling being published frequently. The most relevant published literature has focused on three main areas: computational simulations of the flow field in spinning nozzles, the formation process of air jet spun yarn, and dynamic models of fibers in flow.

Eldeeb and Moučková [6] performed 3D CFD simulations of a Rieter air jet spinning nozzle, presenting the flow field and pressure contours in their results. Several slices of the CFD results were shown, showcasing the high speed regions of air at the orifice, and how the flow field develops as it travels down the length of the nozzle. Simulations, and experiments were performed at different nozzle pressures to gauge the effect on yarn strength, and how the flow field is affected. Guo, An, and Yu [7] performed a similar study on a Murata air jet spinning nozzle, showcasing two-dimensional plots of axial and tangential air velocity at different locations in the spinning chamber.

Some papers were able to create a fluid-solid interaction with the yarn, however they do not discuss how this impacts production rates. Zeng and Yu [8] were able to develop a "ball and bead" model of a fiber, and using a one-way fluid-solid interaction (FSI), they were able to compute the path of the fiber in the nozzle. While the results of the simulation show good correlation to experiments, the model is not able to predict how many fibers interact, or how the path of the fibers can be used to dictate yarn formation. Osman et. al. [9] were able to perform a two-way FSI study on an air jet loom, which is similar in principle to air jet spinning, albeit at a much different scale and with different fiber dynamics. Their results show good correlations with experiments. The most promising study comes from Han et. al. [10], who were able to create a dynamic model for a long, thin, flexible fiber and visualize how it wraps around a stationary core in a flow field representative of what is found in an air jet spinner.

1.2.2 Bladeless Turbines

As previously mentioned, the wavy bladeless turbine is a recent development by Braun et. al., and as such, there is little existing literature on it. As such, the literature review was focused on the potential advantages of a supersonic turbine, and how to best advance the development of this concept.

Traditional bladed turbines have been in use for decades to a great degree of effectiveness, with turbine stages exceeding efficiencies of 90% [11]. As current research revolves around greater fuel efficiency and improved power extraction including technology such as rotating detonation, new methods of power extraction continue to be explored.

Supersonic flow in turbine cascades leads to shockwave formation, greater thermal loads, and reduced efficiency, with experiments by Mee et. al. suggesting shock waves contribute up to 50% of the total losses in a transonic turbine cascade [12]. A limited number of applications currently employ supersonic flow in turbine stages, including turbines used in rocket engines and automotive turbochargers, with proposed designs intended for use in power plants and waste heat recovery [13], [14].

For these reasons, in recent years the concept of a supersonic bladeless turbine has been explored. As discussed previously, some advantages of the bladeless turbine include its dual-purpose operation, acting as both a turbine and supersonic nozzle. Further advantages include wide operational envelope, simplified end wall cooling, and potential integration with rotating detonation combustors (RDCs) [15], [16].

The concept of a wavy bladeless turbine for axial supersonic flows was first published by Braun et. al. [5]. Experimental work was limited to 2D test sections, used to study the pressure distribution across the surface as well as using Schlieren imaging to capture the shock wave and expansion fan formation driven by the wavy geometry. Additional experiments include oil film interferometry, used to measure skin friction, and thermocouple instrumentation to measure wall heat flux with both results correlating well with computational simulations [15].

1.3 Objectives and Methods

For the air jet spinner, currently no publications exist which aim to combine CFD of the spinning chamber, formation process of yarn, and dynamics of the fibers. The primary objective of this thesis is to create a model which can predict yarn production rates based on the results of CFD simulations of the air jet spinning chamber. By combining information from the aforementioned sources, dynamic models of wrap fibers will be created, which predict wrap fiber velocities from CFD data. A numerical approach will be used, with verification cases tested against closed-form solutions to the governing equations to ensure the accuracy of the model. Experimental testing will be done on a Savio Lybra Smartspinner® by modifying the spinning chamber for optical access, using a FASTCAM NOVA high speed camera to capture the yarn formation process. The results from the experimental measurements will be used to validate the proposed models.

For the bladeless wavy turbine, numerous numerical simulations have been performed, and the properties and behavior of it have been well documented. The next step in the development of the turbine is experimental testing, which is the driving goal behind chapter three of this thesis.

The primary objective of this study is to develop and apply analytical models and numerical simulations to guide experimental testing of the bladeless turbine concept, particularly in areas involving turbine sizing, and experimental techniques for power absorption. Alternative turbine geometries will be studied, including the effect of wave amplitude on power generation, and modification of the turbine to take a conical form. This analysis will advance the experimental test campaign of the bladeless turbine, making it suitable for laboratory experiments in cold-flow and hot-flow applications, representative of freestream and engine exhaust conditions respectively.

1.4 Thesis Outline

In Chapter 2 of this thesis, three models are developed to calculate the angular velocities of the wrap fibers used in the yarn formation process. The first model is based on a simplified model of the geometry of the completed yarn. The wrap angle α, yarn diameter D_y and yarn production rate V_t are used to calculate the angular velocity of the wrap fibers. The second and third models use results from CFD simulations to calculate the torque acting on a simplified wrap fiber as a result of the aerodynamic drag it experiences. Using this, the second model calculates the angular velocity at which the wrap fiber experiences zero torque, the so-called equilibrium velocity. The third model calculates the dynamics of the wrap fiber, computing the angular acceleration, velocity, and position of the wrap fiber using ordinary differential equations (ODEs) of the fiber's motion. The results of these models were validated using experimental measurements, which used a spinning chamber modified for optical access, and a high speed camera to measure the angular velocity of the wrap fibers. The results of the experimental measurements show good correlation with the proposed models. Consequences of the wrap fiber's motion are explored, including a theoretical limit to the yarn production velocity as a result of the ultimate tensile strength (UTS) of the material.

Chapter 3 of this thesis investigates the supersonic bladeless turbine, and uses analytical and computational techniques to guide the mechanical design in order to facilitate experimental testing. First, the applicability of various power absorbing devices, including an air-brake, electrical, and inertial dynamometer are discussed. New techniques are developed to generate 3D models of the bladeless turbine using MATLAB. These techniques simplify the creation of the turbine's geometry, and allow for flexibility not previously possible with traditional computer aided design (CAD) tools such as SolidWorks, previously used to generate the turbine. Following this, a sizing study was conducted using non-dimensional parameters typically used to study turbomachinery to explore the effects of the turbine's size on the rotational rate and power output. Using the results of this study, a turbine diameter of 3 cm was selected to coincide with laboratory facilities and capabilities. CFD simulations were run to compute the torque and power output of a novel geometry, suggesting mechanical power outputs of up to 200 W are achievable.

2 Air Jet Spinning

2.1 Introduction

Many previous studies aim to examine the air-flow patterns inside the yarn spinning chamber, and characterize the effects of process variables on the resulting yarn. Metrics such as yarn strength, diameter, hairiness and uniformity have all been correlated to process variables including the air jet inlet pressure, impingement angle and back-pressure [3], [17]. Despite this, one of the most important parameters manufacturers aim to optimize is the production rate of the yarn, and currently no studies exist which aim to model or predict the production rate. To do so, a first-principles approach was taken, using drag and angular momentum equations to predict the velocity of wrap fibers. Simplifying assumptions were made to the overall yarn structure to enable this, as common yarns consist of several fibers interwoven in complex paths as seen in experiments performed in [18].

To compute the wrap velocity of the fibers, both numerical and experimental approaches were employed, focusing on the Savio Lybra Smartspinner®. Some details of the spinning chamber geometry have been omitted at request of the manufacturer, and any figures presented in this work do not accurately depict the geometry of the spinner. For the numerical approach, three avenues were explored; one model based on the geometry of the fully-formed yarn, and two models based on the dynamics of the spinning wrap fiber. First, a geometric model was produced, which estimates the speed of the wrap fibers based on the twist angle of the completed yarn as well as the production or take-up rate. The second model employs a one-dimensional model of the wrap fiber, and calculates the forces and moments acting on it as it travels in the flow field. By expanding this model to include the time dimension, we arrive at the third model. The two dynamic models rely on flow field information produced by CFD simulations, and can be considered a one-way fluid-solid interaction (FSI) simulation.

To validate the computational work, an experimental test campaign was performed using the Savio Lybra air jet spinning nozzle. The experimental methodology consisted of flow measurements, static pressure measurements at various locations, and modifying the nozzle to allow for optical access to the spinning chamber. The yarn production process was captured using a high speed camera at framerates of up to 40000 FPS with the video then analyzed to compute the wrap speed and to qualitatively observe the yarn formation process.

2.2 Air Jet Spun Yarn Physical Structure

Air jet spun yarn consists of wrap fibers and core fibers, with core fibers being oriented axially along the length of the yarn, and wrap fibers wrapping around the core, constraining the core fibers. Previous literature makes distinctions between other roles fibers take in the yarn structure including wild fibers and belly-band fibers, with their primary impact being yarn softness and hairiness [3], [19]. As the primary goals of this work focus on yarn production rates, the discussions in this thesis are limited to core fibers and wrap fibers.

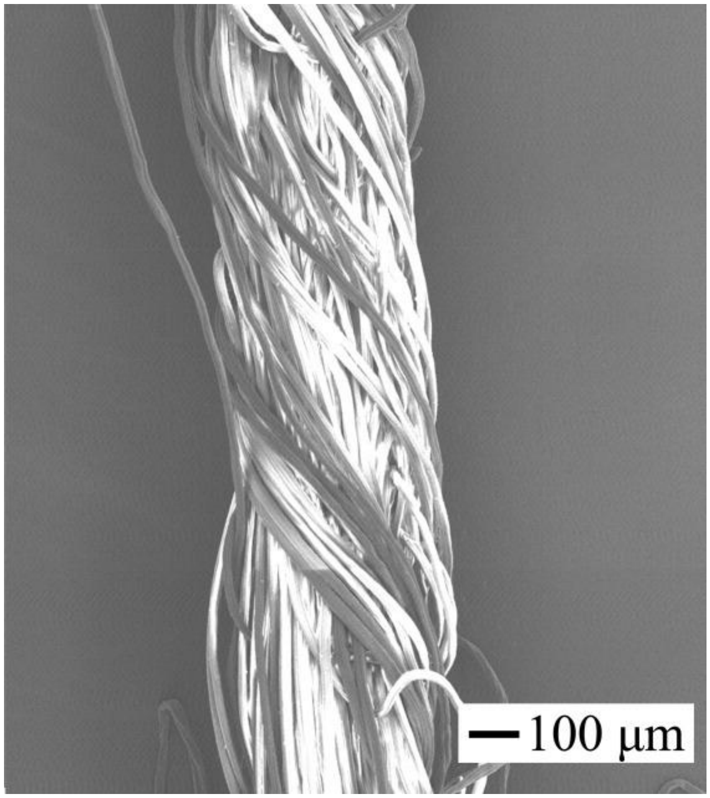

Figure 1. Scanning Electron Microscope (SEM) image of air jet spun yarn. Adapted from [6].

In air jet spun yarn, existing literature suggests that 50%-60% of the fibers exist as core fibers, and 25%-30% are wrap fibers, with the remainder existing as loose or “wild” fibers [20], [3].

To simplify the creation of models of the yarn, a simplified model of air jet spun yarn was created. This model excludes loose fibers, only core fibers and wrap fibers are considered. An additional simplification in the model is that the individual fibers are continuous. In reality, individual fibers vary in length from 30mm to 50mm in length, taking complex and interwoven paths as they wrap around the core and themselves. This idealized model of yarn is consistent with existing literature, including work from Samy et. al. and Kremenakova [21], [22]. Images of the simplified yarn model are shown below.

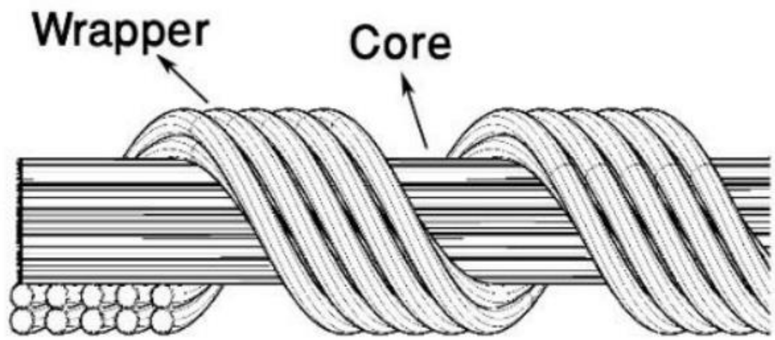

Figure 2. Simplified model of air jet spun yarn, adapted from [8].

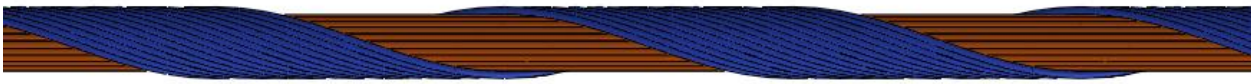

Figure 3. CAD model of simplified yarn structure with scale dimensions.

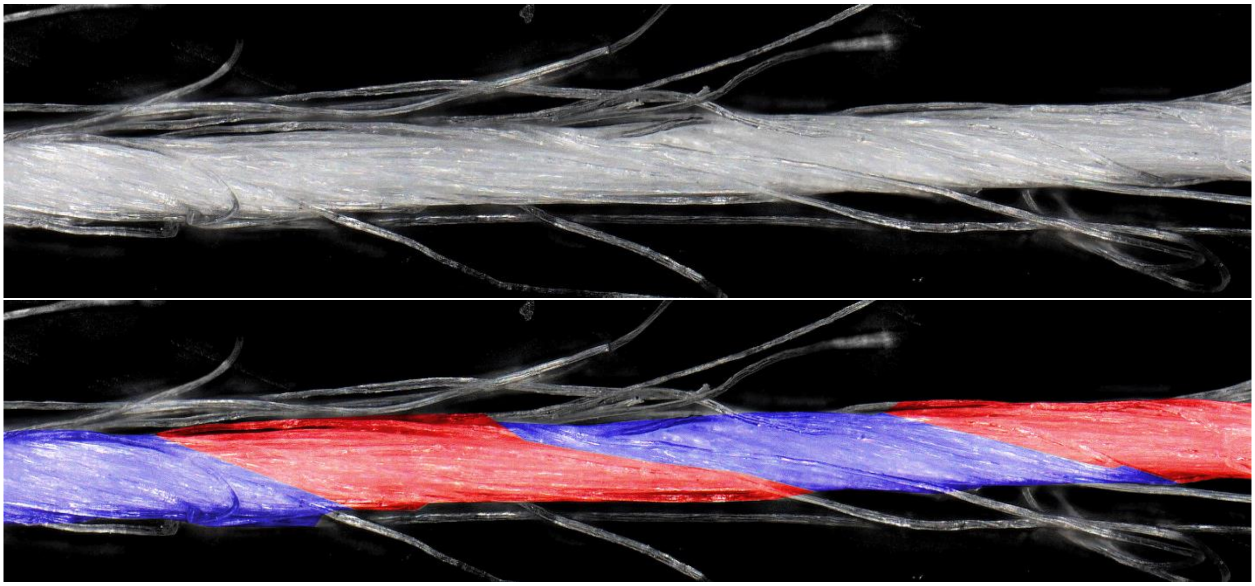

Figure 4. Images of yarn structure produced by Savio Lybra. A) Unaltered image. B) Color coded to illustrate core fibers (red) and wrap fibers (blue).

Existing literature and patents from Murata outline a similar, but slightly different wrap model. In this model, all wrap fibers begin as core fibers, slowly migrating to the yarn's surface before emerging and ending as a wrap fiber. This has been tested through experimental means both through the insertion of tracer fibers which are manually tracked after being spun into a yarn, and through new techniques such as Digital Volumetric Imaging [23]. Analysis of this yarn structure have been performed by Zou et. al., and arrive at similar conclusions for the wrap velocity presented in this thesis [24].

2.3 Yarn Formation in Air Jet Spinning

Numerous sources including [3], [25], and [7] describe the air jet spinning process in great detail, and so some details will be omitted from this simplified explanation for brevity. To begin, staple fibers are brought into the spinning chamber through feed rollers and suction generated at the inlet. Following this, a portion of the loose fibers are separated from the main core, these will become the wrap fibers. The wrap fibers are oriented perpendicular to the main core fibers in the radial direction, with some patents suggesting they fold backwards over the spindle, with the free end oriented axially. Jets of air, aimed roughly tangentially to the production direction of the yarn, impart a torque on the wrap fibers, spinning them around the core fibers. This results in a fully formed yarn, with core fibers that are oriented axially, and wrap fibers that wrap around and constrain the core, oriented at a wrap angle α with reference to the yarn's axial direction. The completed yarn is fed through a series of pulleys to maintain a constant tension, before being spooled onto the final bobbin using a series of rollers.

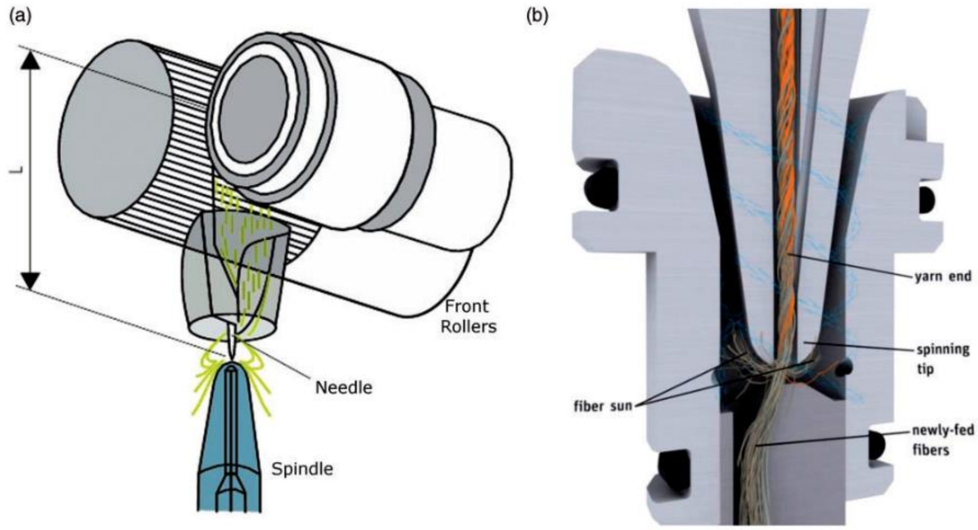

Figure 5. Detailed view of yarn formation in air jet spinning a) Murata Vortex Spinning, b) Rieter jet spinning. Adapted from [12].

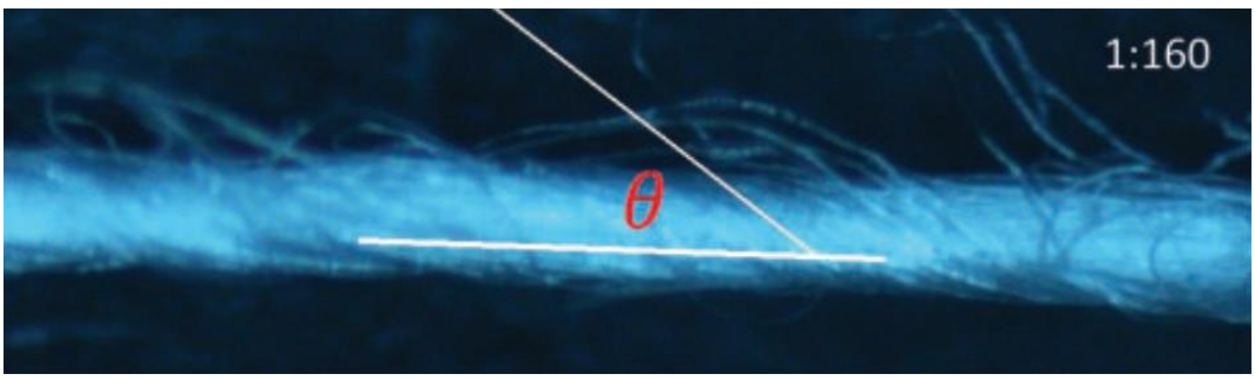

Figure 6. Air jet spun yarn showcasing wrap angle. Adapted from [10].

2.4 Geometric Model of Wrap Fiber Velocity

The first model created to estimate the rotational rate of the wrap fiber was based on the geometry and production rate of a completed yarn. The outer circumference of the yarn is unwrapped to more clearly visualize the path of the wrap fibers as shown below.

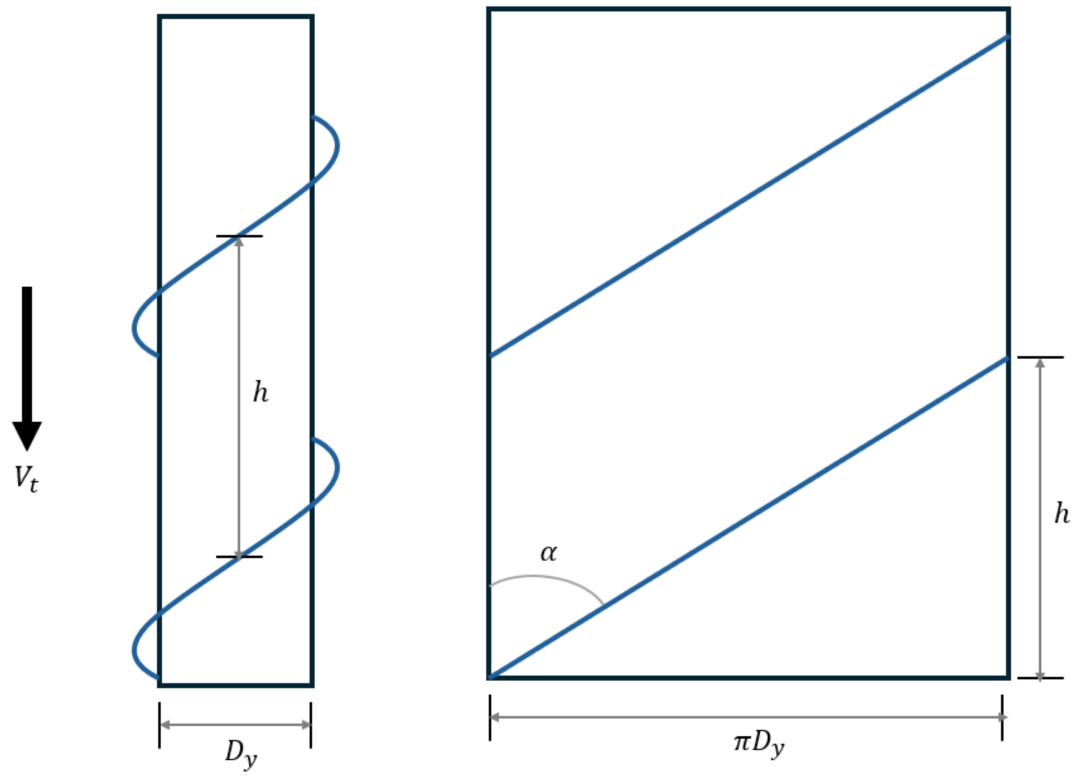

Figure 7. Diagram of yarn with wrap fiber (left), unrolled (right).

This simplified yarn model has been used by other authors in the past, including Kremenekova [22], and Karakan et. al. [3], with Zou et. al. presenting similar results after conducting experimental analyses [26].

The production rate, or take-up velocity of the yarn is denoted by V_t. By inspection, it can be seen that the wrap fiber must make one complete revolution around the yarn core in the time it takes the yarn to travel distance h. The distance the wrap fiber travels in the tangential direction around the yarn is πD_y, meaning the tangential velocity of the wrap fiber at the yarn surface is equal to the following.

$$u_t = \frac{\pi D_y}{\frac{h}{V_t}} = \frac{V_t \pi D_y}{h} = V_t \tan(\alpha)$$

Converting the tangential velocity of the wrap fiber to an angular velocity can be done by dividing by the radius of the yarn, giving the following equation.

$$\dot{\theta} = \frac{V_t \tan(\alpha)}{\frac{1}{2} D_y} = \frac{2V_t \cdot \tan(\alpha)}{D_y}$$

This conclusion, while developed independently, is the same one presented by Zou et. al. in [24] for regular wrap fibers, the term the authors use for wrap fibers which exist at the surface of the yarn.

2.5 Computational Simulations of Air Flow in Spinning Chamber

As mentioned in 1 Introduction, many previous studies performed CFD simulations to study the air flow patterns in the spinning chamber. These studies served as reference material to begin the CFD simulations outlined in this thesis.

In general, CFD simulations aim to solve the following equations using a discretized air domain [27].

Conservation of mass:

$$\frac{\partial \rho}{\partial t} + \nabla \cdot \left(\rho \vec{V}\right) = 0$$

Conservation of momentum (Navier-Stokes equation):

$$\frac{\partial \vec{V}}{\partial t} + \vec{V} \cdot \nabla \vec{V} = -\frac{\nabla p}{\rho} + \nu \nabla^2 \vec{V} + \vec{f}_b$$

Conservation of energy:

$$\frac{\partial (\rho h_{tot})}{\partial t} - \frac{\partial p}{\partial t} + \nabla \cdot \left(\rho \vec{V} h_{tot}\right) = \nabla \cdot (\lambda \nabla T) + \nabla \cdot \left(\vec{V} \cdot \tau\right) + S_E$$

Additional information regarding the CFD setup is discussed in later sections.

2.5.1 Fluid Domain Generation

The first step in performing CFD simulations is to create the fluid domain. This was done using SOLIDWORKS 2023. Computer-aided design (CAD) models were provided by the manufacturer of the nozzle, and SOLIDWORKS was first used to convert the .step files to native .part files. A fluid domain was then created using tools such as fill, delete face and boolean operators. After completing the initial geometry, some changes to the domain were made to ensure the boundary conditions imposed by the CFD software could be adhered to. Namely, this consisted of adding plenum volumes to air inlets and outlets. Following this, the fluid domain is complete, and the geometry was exported to a .step file to import in the meshing software.

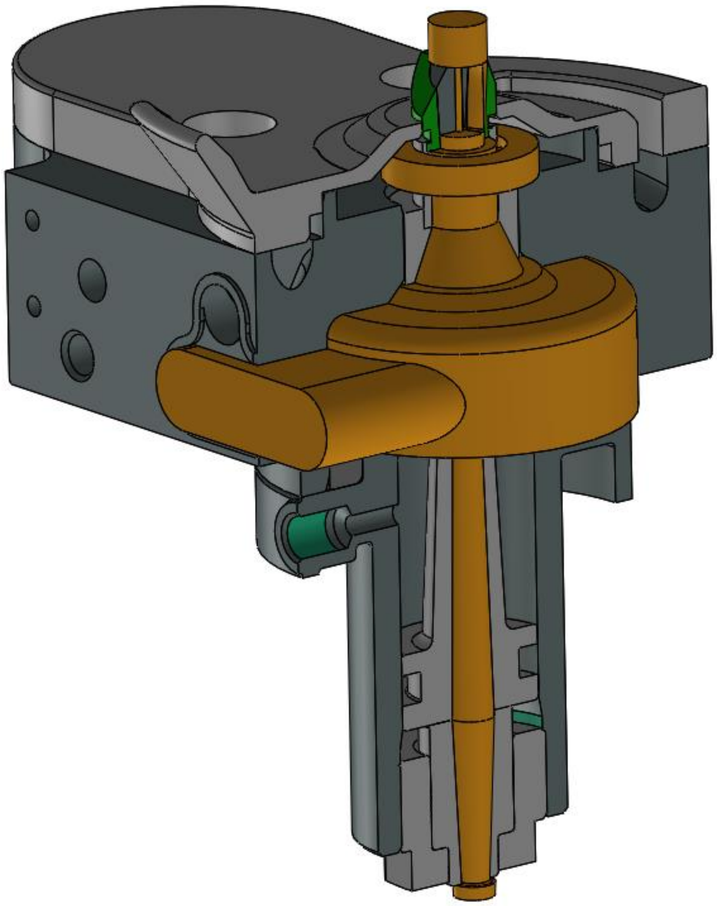

Figure 8. Cross sectional-view of nozzle, with fluid domain shown in orange.

2.5.2 Mesh Generation

Meshing is the process of discretizing the solid volume into a number of individual cells before using the mesh to perform CFD. This was performed using a commercial software, Numeca HEXPRESS. Phung et. al. describe using ANSYS CFX to generate the mesh and perform the CFD simulation, using a cell count of approximately two million [28]. Guo, An, and Yu, as well as Eldeeb, and Moučková both separately describe using ANSYS FLUENT to generate meshes of approximately 200 000 cells and 500 000 cells respectively [7], [6]. With the progression of computing power since the publishing of those papers, a cell count not exceeding 20 million was suggested. One of the meshes used for the CFD simulations is shown below, with a cell count of 16 million.

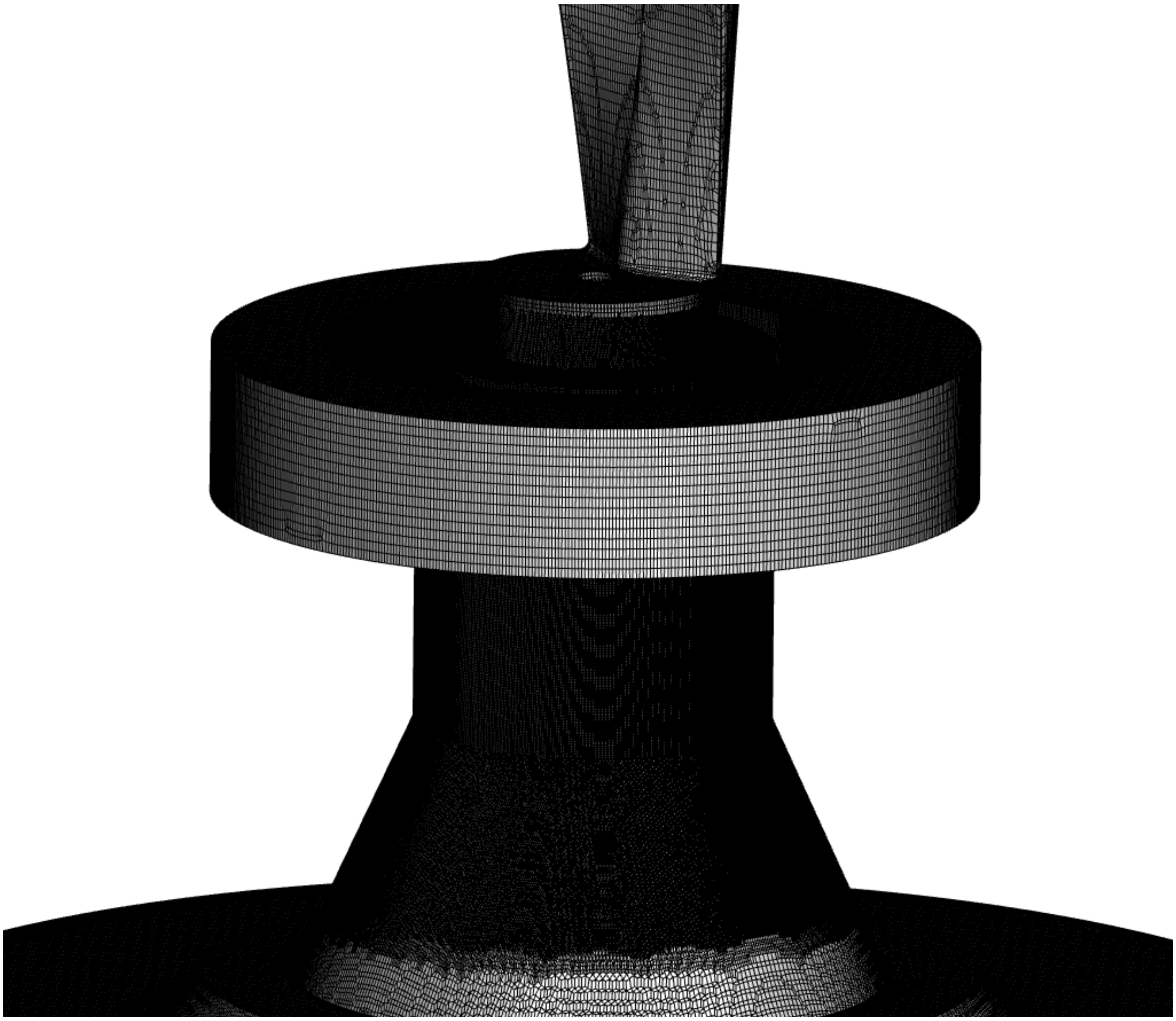

Figure 9. Mesh used for air jet spinner CFD simulations.

Another important aspect of mesh generation for CFD is wall refinement, where viscous effects of the fluid flow can be captured. The metric most commonly used to study wall refinement is y^{+}, which is a non-dimensional number which describes the ratio between the product of the free-stream fluid velocity, fluid density, and nodal distance to the fluid's dynamic viscosity. To accurately resolve the viscous interactions between fluid flow and a wall, a y^{+} value below 1 is commonly cited when using a $k - \omega\, SST$ turbulence model, allowing the boundary layer to be accurately modeled. An equation for y^{+} is shown below.

$$y^{+} = \frac{\rho y_p u_t}{\mu}$$

If the free-stream fluid velocity is known, the equation can be used to calculate the wall spacing. This wall spacing can be passed as a parameter in HEXPRESS, where the software will then use this as a target cell size for cells bordering the walls of the simulation domain. A cell inflation ratio of 1.2 was used for the viscous layer insertion process. This limits the aspect ratio of neighboring cells, making the simulation more stable.

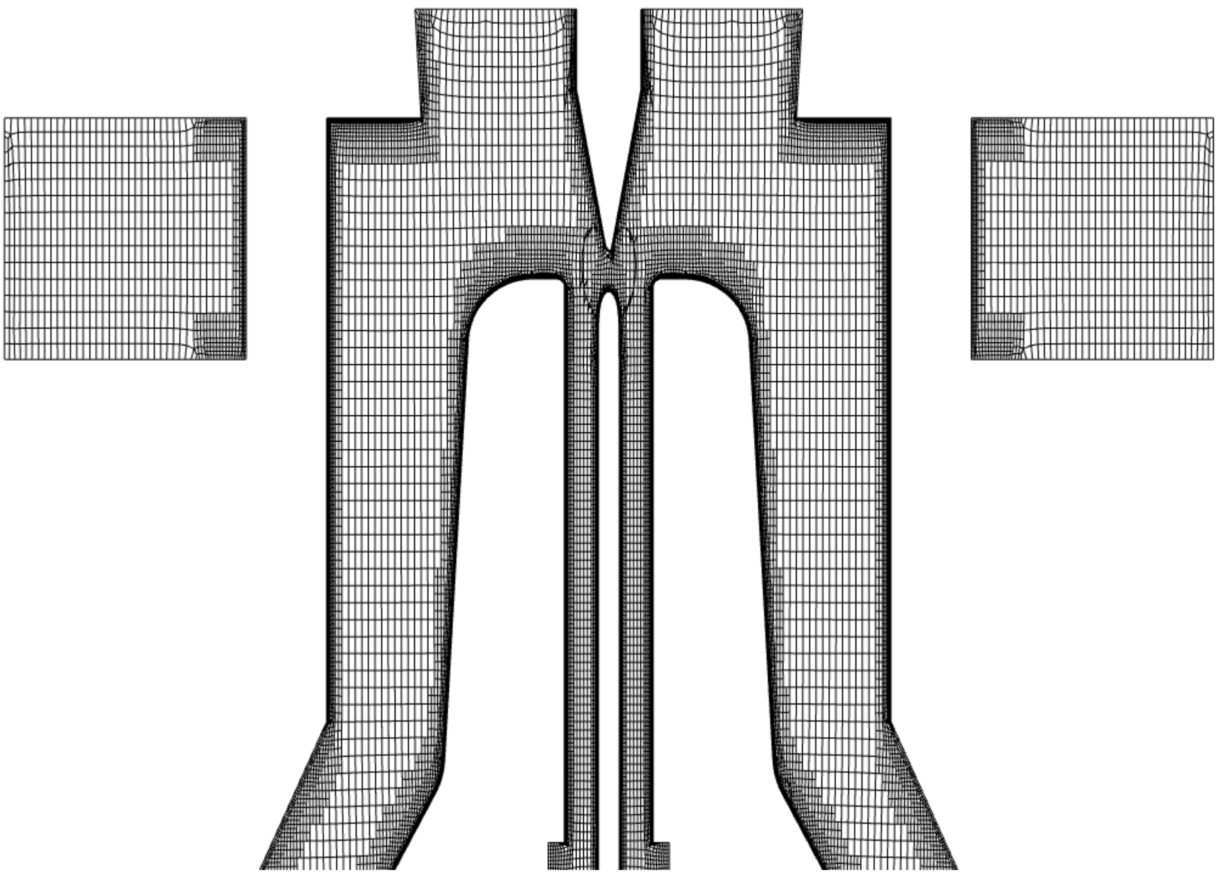

Figure 10. Section view of spinning chamber showing mesh. Viscous inflation layers can be seen near the outer contour of the domain.

It is advantageous to reduce the cell count of the mesh as the computational time is reduced, however doing so may lead to artifacts in the flow field which are not present in the real world. To reduce the cell count, refinement regions were specified around areas of interest of the nozzle, primarily the region in which the fibers are spun. Doing so reduces the cell size, ensuring flow features are captured more accurately in this region, while reducing the complexity of the mesh in regions where the flow does not need to be accurately resolved, such as the inlet and outlet plenums.

2.5.3 CFD Simulations and Results

To set up and solve the computational simulations, Metacomp Technologies' iCFD++ was used due to its ability to be easily automated, and stability when working with supersonic flows [29].

All simulations were run using a steady-state Reynolds Averaged Navier-Stokes (RANS) turbulence simulation type, using a two equation $k - \omega\, SST$ turbulence model. This model was chosen for its suitability for use with internal viscous flows. No laminar simulations were run due to the turbulent nature of the spinning chamber. This was verified by calculating the Reynolds number in the chamber, which was consistently found to be above 30000, safely in the turbulent regime. This conclusion was also discussed by Pei and Yu [30].

The majority of the fluid domain's walls were specified as viscous walls to capture the formation of a boundary layer. The air plenums that supply the jets in the spinning chamber were specified using stagnation pressure and temperature. The specific values were set to the default values used during operation of the Savio Lybra, namely 6 bar absolute inlet pressure, and 295 K temperature. The air outlets of the spinning chamber were specified using characteristics-based boundary conditions with a pressure of 1 bar.

To solve the CFD simulations, the cases were parallelized and run on the NCSU High-Performance Computing (HPC) cluster. The simulations were run using 64 cores and took approximately 24 hours before they were deemed converged. Future simulations focused just on the spinning chamber used a smaller air domain with a lower cell count, taking only 6 hours to run on 32 cores, while achieving a similar level of accuracy.

2.6 Dynamic Model of Wrap Fiber

As previously mentioned, while existing research that performed computational simulations of the airflow in the spinning nozzle and chambers exist, no authors mention the ability to connect these simulations to measurable results such as yarn production rates, or fiber wrap angles. In order to do so, a dynamic model of a wrap fiber was developed such that results from the computational simulations, including air density and velocity could be used to calculate the motion of the wrap fiber. Previous publications mention the use of a "ball and chain" model, where fibers are modeled as individual segments attached through elastic links with corresponding bending and elastic stiffnesses [31]. While the authors demonstrate success in coupling this model with the fluid simulations, they were limited by it in that there were only able to plot the motion of a single fiber as it traveled through the nozzle in a path which is unrepresentative of the wrapping process.

Developing a model which is capable of accounting for the complex motion of the wrap fiber, including bending, twisting, buckling, and interactions with other fibers would prove very challenging, and as such, some simplifying assumptions were made to assist in the creation of the new wrap-fiber model.

The first assumption is that the wrap fibers behave as short segments 2 mm in length, with one end fixed along the central axis of the yarn, while the other end is free to move.

The second assumption is that the wrap fibers spin in-plane about the yarn's central axis. Previous patents suggest that the wrap fibers extend downstream past the tip of the spindle, however after performing analysis of the high speed video, this was not observed in the Savio machine. As a result of this, it is assumed that the wrap fibers spin in-plane about the yarn's central axis, extending 2 mm in the radial direction. The length of the wrap fiber was found to have a significant impact on the results of dynamic models, however the 2 mm length was selected based on experimental measurements, giving good results of the fiber wrap velocity. Furthermore, the length of the wrap fiber is limited to the radius of the spinning chamber, approximately 3 mm.

The third assumption is that the short wrap-fiber segment behaves as a rigid cylindrical bar which does not bend or deform in any way.

This model is limited in the fact that the motion of the fiber is not coupled to the CFD simulations; from the point of view of the CFD solver, the fibers do not exist. The fluid-solid interaction occurs only from the CFD to the fiber model. This assumption was made on the basis that the individual fibers are on orders of magnitude smaller than the spinning chamber (μm vs mm). Simulations were run using a modified mesh geometry which included the presence of the simplified yarn model presented earlier, with minimal impact in the flow field being noted.

The goal of the fiber dynamic model is to accurately calculate the torque acting on the fiber in the wrapping plane. With these assumptions in place, the equations of motion of the fiber can be developed, and the dynamics of the wrap fiber can be solved.

To calculate the forces and moments, the fiber is discretized into short segments, taking inspiration from blade element theory (BET) commonly used in the analysis of aircraft propellers and wind turbine rotors. An illustration is shown below.

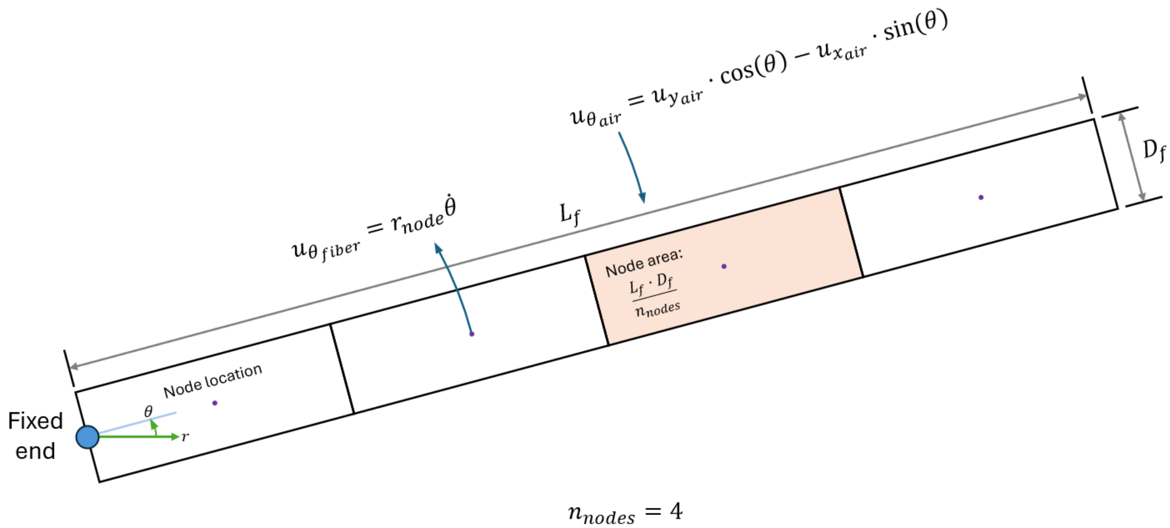

Figure 11. Diagram of fiber nodes, areas, and velocities.

Forces and moments are calculated on the fiber elements using properties including air density, relative velocity, and node frontal area.

The following coordinate system is used for the presentation of the CFD results, and fiber wrap velocity models. The wrap fiber rotates about the z-axis. When projected on to the x-y plane, the angle formed between the wrap fiber and the x-axis is θ.

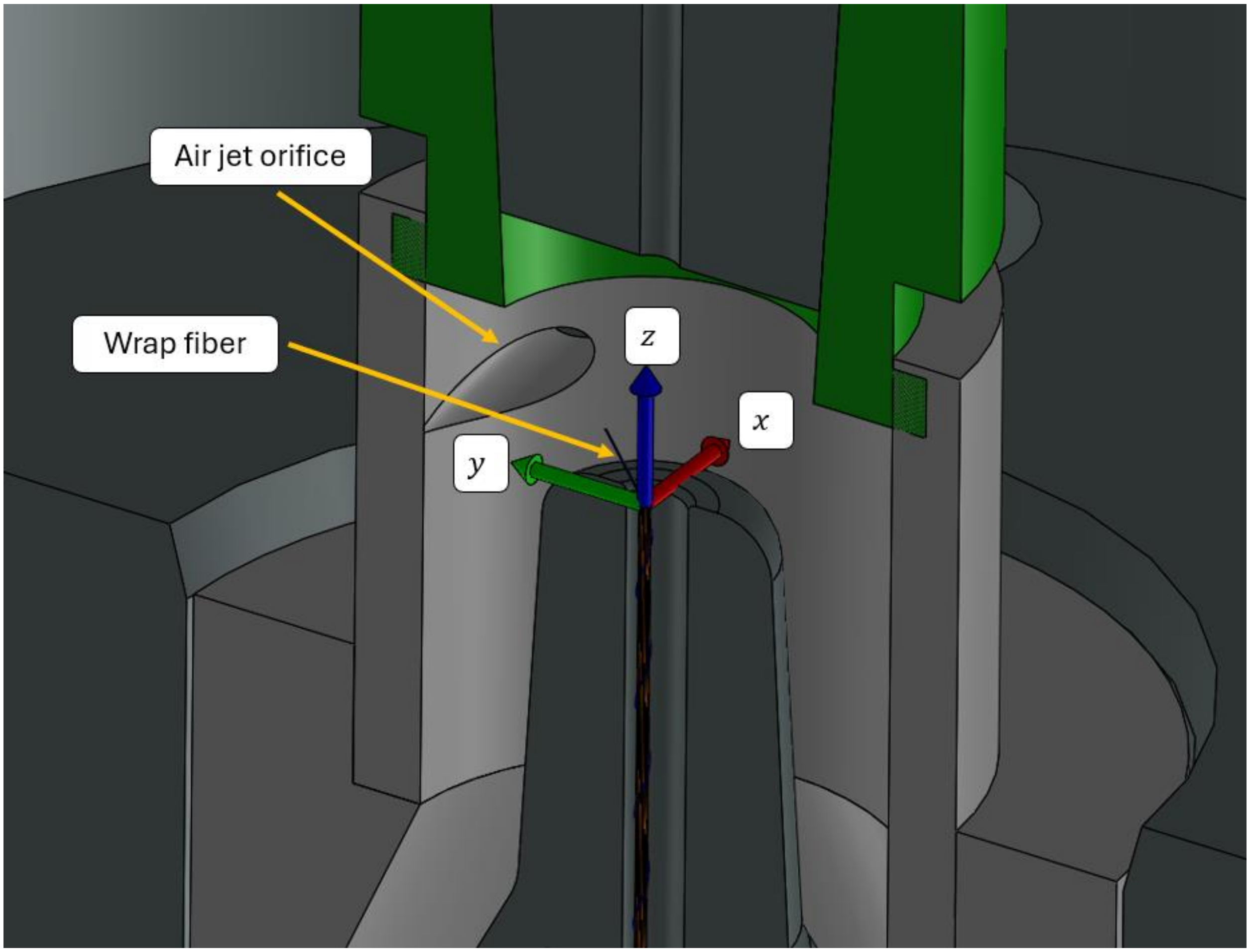

Figure 12. Coordinate system used for presentation and discussion of results.

2.6.1 Fiber Equations of Motion

With the model simplifications of the dynamic model established, the equations of motion of the individual fiber can be developed.

From Newton's second law for rotational motion where τ represents torque, $\ddot{\theta}$ represents the angular acceleration, and I represents the object's moment of inertia, we have:

$$\sum \tau = \ddot{\theta} I$$

The fibers are modeled as circular cylinders. For a uniform cylinder with mass m and length l rotating about its end, the moment of inertia is:

$$I = \frac{1}{3}ml^2$$

The velocity at any point on the fiber is equal to the radial distance multiplied by the angular velocity:

$$u_{\theta_{fiber}} = r\dot{\theta}$$

As the CFD computations were performed in cartesian coordinates, when converting to polar, they become the following:

$$u_{\theta_{air}} = u_{y_{air}} \cdot \cos(\theta) - u_{x_{air}} \cdot \sin(\theta)$$

The relative velocity along the tangential direction between the fiber and the air then becomes the following:

$$V_{rel} = u_{\theta_{air}} - \dot{\theta}r = u_{y_{air}} \cdot \cos(\theta) - u_{x_{air}} \cdot \sin(\theta) - \dot{\theta}r$$

Drag is modeled with the following equation, where F_d is the force of drag, ρ is the fluid density, C_d is the drag coefficient, A is the cross-sectional area exposed to the flow, and V_{rel} represents the relative air velocity:

$$F_d = \frac{1}{2}\rho C_d A V_{rel}^2$$

To calculate the torque acting on the fiber, the aerodynamic drag is multiplied by the radial distance along the fiber:

$$\tau_d = \frac{1}{2}\rho C_d A V_{rel}^2 r$$

Since the previous equation is scalar in nature, the magnitude of the relative velocity is used to calculate the direction in which the torque acts. This equation forms the basis of the fiber's rotational dynamics model, used in both 1D and 2D implementations:

$$\tau_d = \mathrm{sgn}(V_{rel})\frac{1}{2}\rho C_d A V_{rel}^2 r$$

From the assumptions made when developing the simplified model, the only torque acting on the fiber is that due to aerodynamic drag. The final equation of motion of the fiber then becomes:

$$I\ddot{\theta} = \mathrm{sgn}(V_{rel})\frac{1}{2}\rho C_d A V_{rel}^2 r$$

This is a second order ordinary differential equation (ODE) with some closed form solutions for simple distributions of ρ, C_d, and V_{rel}.

2.6.2 Drag Force on Fiber

The total drag torque acting on the fiber can be calculated in a closed-form solution for simple velocity fields. For a uniform zero-velocity field, the relative velocity is defined with the following equation.

$$V_{rel} = u_{\theta_{air}} - \dot{\theta}r = -\dot{\theta}r$$

The derivation for the total drag torque is shown below.

$$d\tau_{exact} = \frac{1}{2} \cdot \rho \cdot V_{rel}^2 \cdot r \cdot C_d \cdot D_f \cdot dr$$

$$d\tau_{exact} = \frac{1}{2} \cdot \rho \cdot \left(-\dot{\theta}r\right)^2 \cdot r \cdot C_d \cdot D_f \cdot dr$$

$$\tau_{exact} = \frac{1}{2} \cdot \rho \cdot C_d \cdot D_f \cdot \dot{\theta}^2 \cdot \int_0^r r^3 \cdot dr$$

$$\tau_{exact} = \frac{1}{8} \cdot \rho \cdot C_d \cdot D_f \cdot \dot{\theta}^2 \cdot r^4$$

In both fiber dynamic models discussed in the following sections, one commonality is that the wrap fiber is discretized into small sections spanning the radial length. The total drag force acting on the fiber can be found by taking the sum of the individual contributions of each fiber section, or through other means such as a trapezoidal integral approximation if the data is correctly normalized. By discretizing the fiber into a sufficient number of sections, the forces and torques that are calculated from the previous equations converge to a number representing the actual force acting on the fiber. The table below demonstrates how an increasing number of fiber segments converges on the closed-form solution of a fiber rotating at $\omega = 100\,\frac{\text{rad}}{\text{s}}$ in a uniform static velocity field with $\rho = 1\,\frac{\text{kg}}{\text{m}^3}$, $C_d = 1$, $D_f = 0.02$mm, and $r = 2$mm. For simulations using the flow field calculated by the CFD, a fiber node count of $n = 1000$ was used.

Table 1. Fiber node count sensitivity study.

Fiber node count n_{fiber}	Approximate solution τ_{appr}	Percent error $\frac{\lvert\tau_{appr}-\tau_{exact}\rvert}{\tau_{exact}} \cdot 100\%$
5	$3.92 \cdot 10^{-13}$Nm	2%
10	$3.98 \cdot 10^{-13}$Nm	0.5%
50	$3.9992 \cdot 10^{-13}$Nm	0.2%
100	$3.9998 \cdot 10^{-13}$Nm	0.005%

One important parameter that has not been discussed is the drag coefficient of the fiber. In the simplified dynamic model, the fibers are represented by long, straight cylinders and as such, the drag coefficient for a cylinder in crossflow was selected for use. The drag coefficient for cylinders in crossflow has been verified experimentally by numerous authors in the past, with Anderson et. al. presenting the following data.

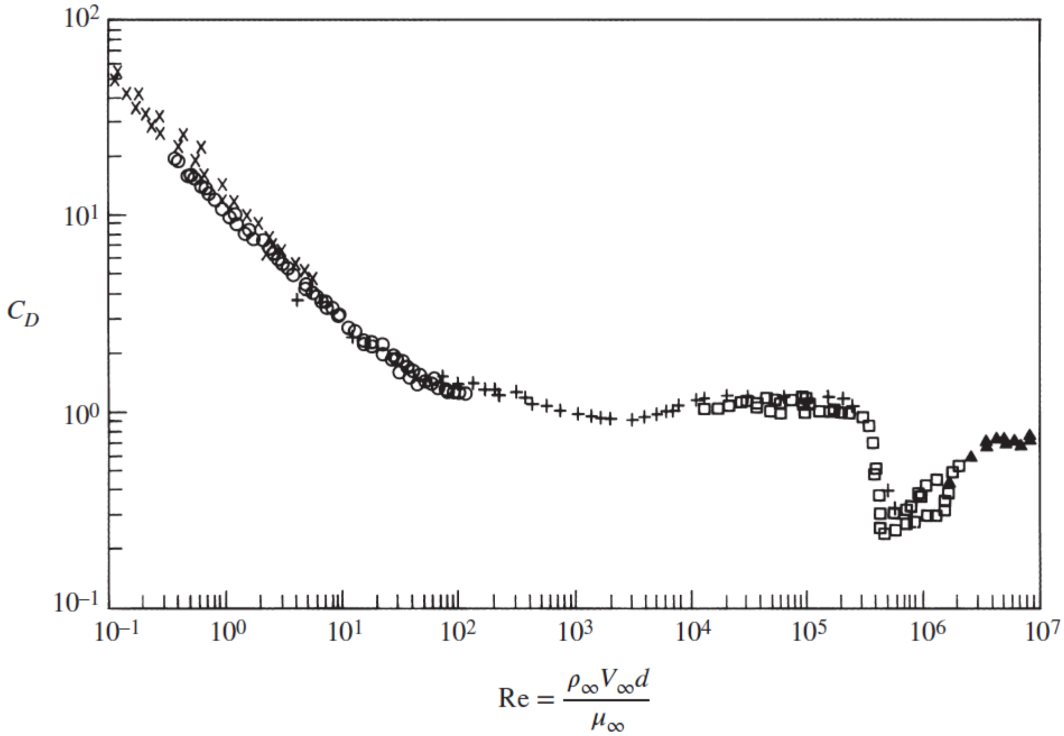

Figure 13. Plot of drag coefficient of a cylinder vs. Reynolds number. Adapted from [17].

As can be seen, a strong correlation between the Reynolds number and the drag coefficient exists. Reynolds number defines the ratio of inertial to viscous forces in a fluid flow [1], and commonly takes on values from zero to tens of millions for large objects traveling at high speeds through free-flowing fluids such as airliners. Due to the small scale of the individual fibers being spun, it can be safely assumed that the flow field around them is laminar, despite the turbulent flow found in the spinning chamber. This hypothesis was validated during the 1D and 2D simulations of the fiber's motion, where the Reynolds number rarely exceeded 50.

Finn and Wieselsberger conducted experiments measuring the drag coefficient of circular cylinders in laminar flows from Re = 0.1 to Re = 80 [32], [33]. As suggested by Potts, several reputable sources were in strong agreement with this data, including Lamb, Relf, Eisner, Schiller and Linke, Pechstein and others [34]. Plotting the data for drag coefficient as a function of Reynolds numbers between 0 and 80 yields the following graph.

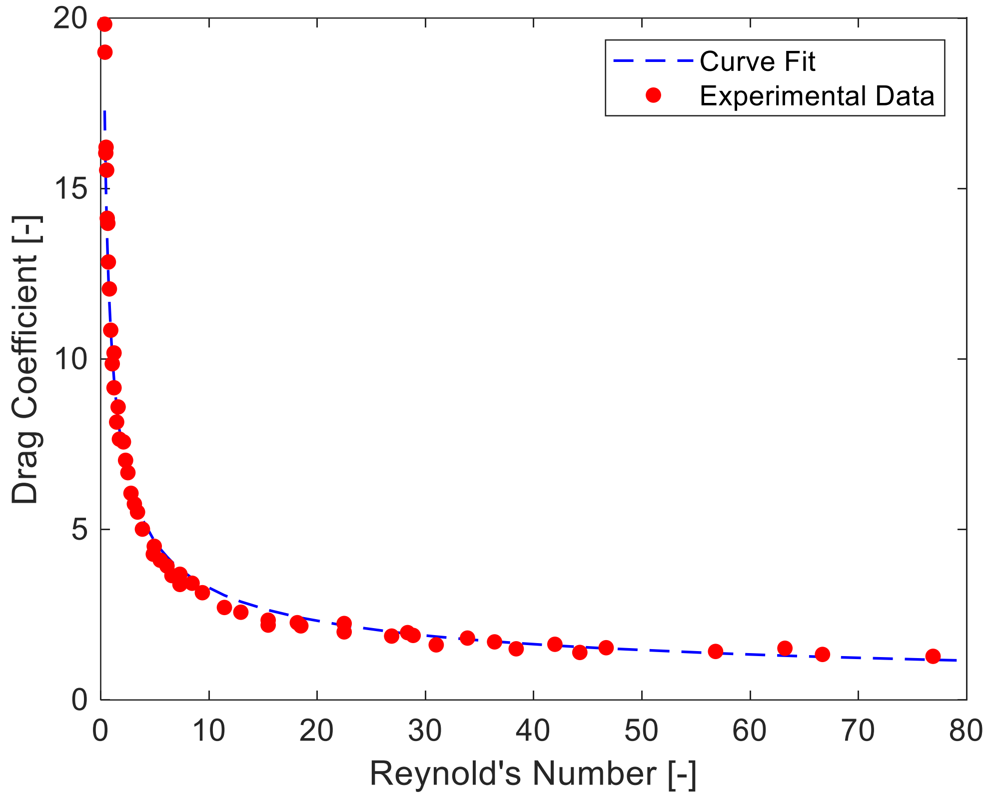

Figure 14. Cylinder drag coefficient as a function of Reynolds number, data obtained from [32], [33].

A power function was fitted to the data, yielding an empirical relationship with $R^2 = 0.992$.

$$C_d = 10.4454\ \mathrm{Re}^{-0.5028}$$

2.6.3 1D Model

Initially, a one-dimensional model was used to calculate the equilibrium velocity of the fiber with respect to its angular position in the spinning chamber. The equilibrium velocity is defined as the rotational velocity of the wrap fiber at which the total torque on the fiber caused by aerodynamic drag is equal to zero. To calculate this velocity, slices of data were extracted from the CFD solution at varying heights, representing the spinning plane. An angle was specified to the fiber, and from this, the location of the fiber nodes could be calculated by converting the polar coordinates to cartesian. The cartesian coordinates of the fiber nodes were then used to calculate the tangential air velocity, and air density from the CFD results, using a linear interpolation with the *griddata* function in MATLAB. Knowing the tangential air velocity, the rotational velocity of the fiber can be solved iteratively to yield a relative velocity distribution that results in no net torque on the fiber. Once this was complete, a new angle was selected and the process was repeated. The result of this model is a plot of fiber angle vs equilibrium velocity.

2.6.4 2D Model

The two-dimensional model operates in a similar fashion to the one-dimensional model discussed previously. Instead of calculating the fiber velocity at which the net torque is zero, the two-dimensional model uses the fiber's current position and angular velocity to calculate the resulting torque. With the torque, the angular acceleration can be found using the fiber's equations of motion. Using MATLAB's built-in ordinary differential equation (ODE) solver *ode45*, a small timestep is used to calculate the fiber's new velocity and position. The fiber's new velocity is incremented using the following equation:

$$\ddot{\theta} \approx \frac{\Delta\dot{\theta}}{\Delta t}$$

Similarly, the fiber's new position is calculated using the following equation:

$$\dot{\theta} \approx \frac{\Delta\theta}{\Delta t}$$

The result of this model is the fiber's angular position, velocity, and acceleration as a function of time. These results can also be plotted against each other to yield graphs of the fiber's velocity as a function of position in the spinning chamber, which is useful to correlate with the geometry of the spinning chamber including the air jets and fiber inlet.

As mentioned previously, some closed form solutions of the fiber's equation of motion exist for simple flow fields. To evaluate the accuracy of the solution produced by MATLAB's *ode45*, a solution was derived for the stationary flow field used earlier to validate the fiber node discretization. The derivation is as follows:

Previously, the torque acting on the fiber in a stationary flow field was found to be the following. The drag torque will always be acting in the direction opposing the fiber's motion, giving the negative sign not seen previously:

$$-\frac{1}{8} \cdot \rho \cdot C_d \cdot D_f \cdot \dot{\theta}^2 \cdot r^4$$

Combining this with the fiber's equation of motion gives the following:

$$I\ddot{\theta} = -\frac{1}{8} \cdot \rho \cdot C_d \cdot D_f \cdot \dot{\theta}^2 \cdot r^4$$

The constants can be combined to form:

$$\ddot{\theta} = -\frac{\rho \cdot C_d \cdot D_f \cdot r^4}{8 \cdot I} \cdot \dot{\theta}^2 \Rightarrow \ddot{\theta} = A\dot{\theta}^2$$

This is a simple first-order ODE with the following solution, with $\dot{\theta}_0$ representing the initial condition, the fiber's velocity at time $t = 0$.

$$\dot{\theta}(t) = \frac{\dot{\theta}_0}{1 - \dot{\theta}_0 At}$$

Plotting the exact solution against the solution generated by *ode45* yields the following:

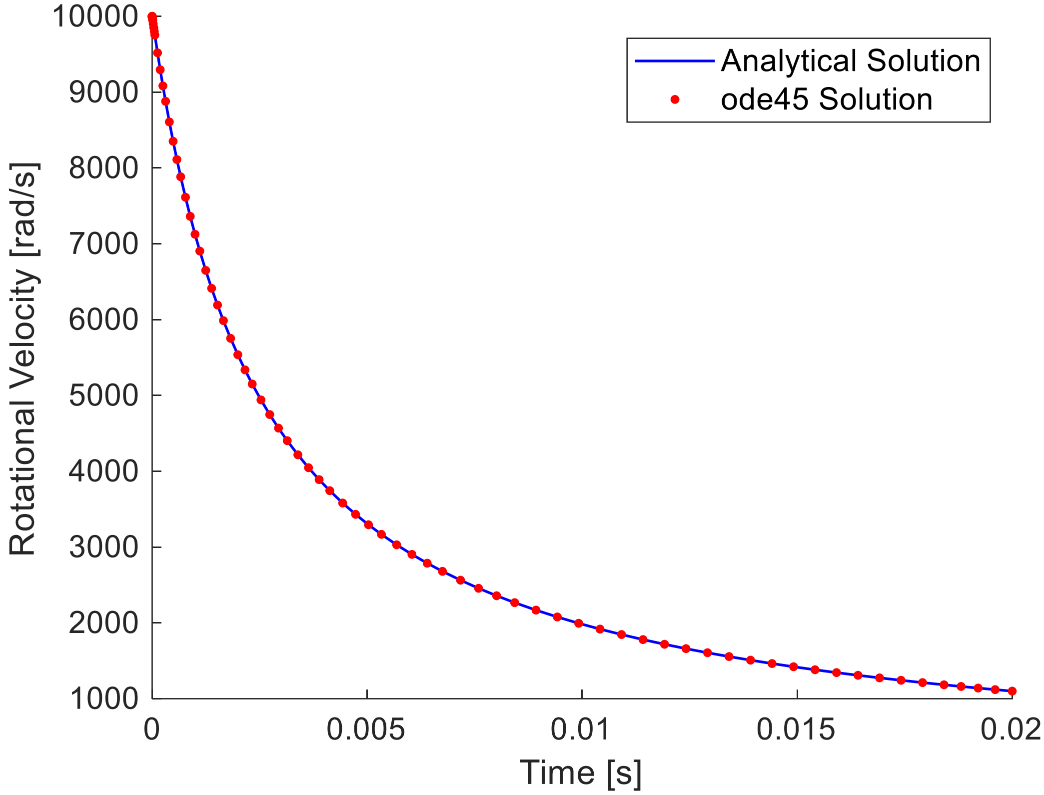

Figure 15. Fiber velocity vs time in uniform static fluid field with $\dot{\theta}_0 = 10000 \frac{\text{rad}}{\text{s}}$.

2.7 Results

To calculate the angular velocity of the wrap fiber using the geometric model, production data and microscope images of yarn produced using the Savio spinner was obtained. Using the provided scale, the yarn diameter D_y and wrap angle α were computed.

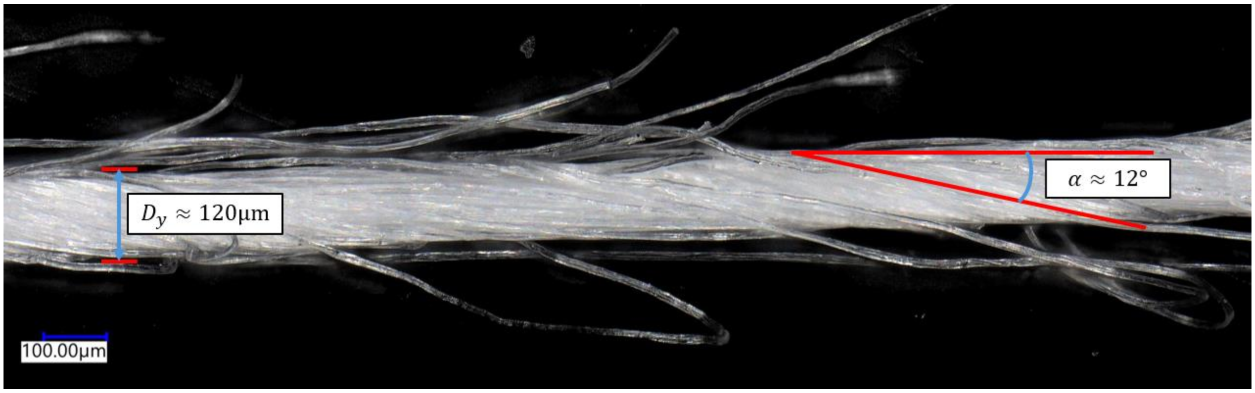

Figure 16. Microscope image of yarn produced by Savio Lybra spinner.

Using these results, the wrap fiber rotational velocity was found to be the following.

$$\dot{\theta} = \frac{2V_t \cdot \tan(\alpha)}{D_y} = \frac{2 \cdot 7.5\frac{\text{m}}{\text{s}} \cdot \tan(12°)}{120 \cdot 10^{-6}\text{m}} \approx 26600\frac{\text{rad}}{\text{s}}$$

This result is in line with other sources, including Krause and Nakahara, who suggest rotational rates of wrap fibers between $15000\frac{\text{rad}}{\text{s}}$ and $31000\frac{\text{rad}}{\text{s}}$ [35], [36]. Due to the age of their publications, and continued developments in air jet spinning allowing for faster production rates, with some manufacturers claiming up to $500\frac{\text{m}}{\text{min}}$, it is possible that the upper bound could be exceeded.

A slice of the CFD results taken at the spinning plane is shown below. The plotted variable, the tangential velocity, demonstrates how the two air jets located at $90°$ and $270°$ create a strong swirling flow in the spinning chamber. Simulation results like these ones were used in the one-dimensional and two-dimensional fiber dynamic models to compute the velocities of the wrap fiber.

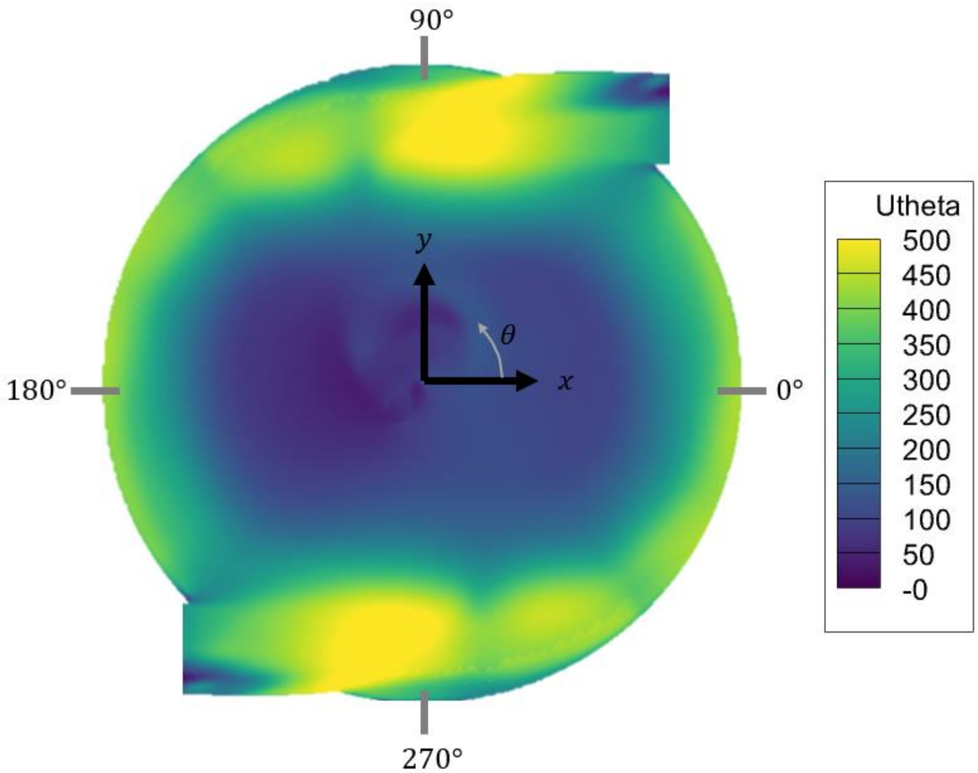

Figure 17. CFD results of tangential air velocity in spinning chamber.

An example result of the one-dimensional fiber dynamic model is shown below.

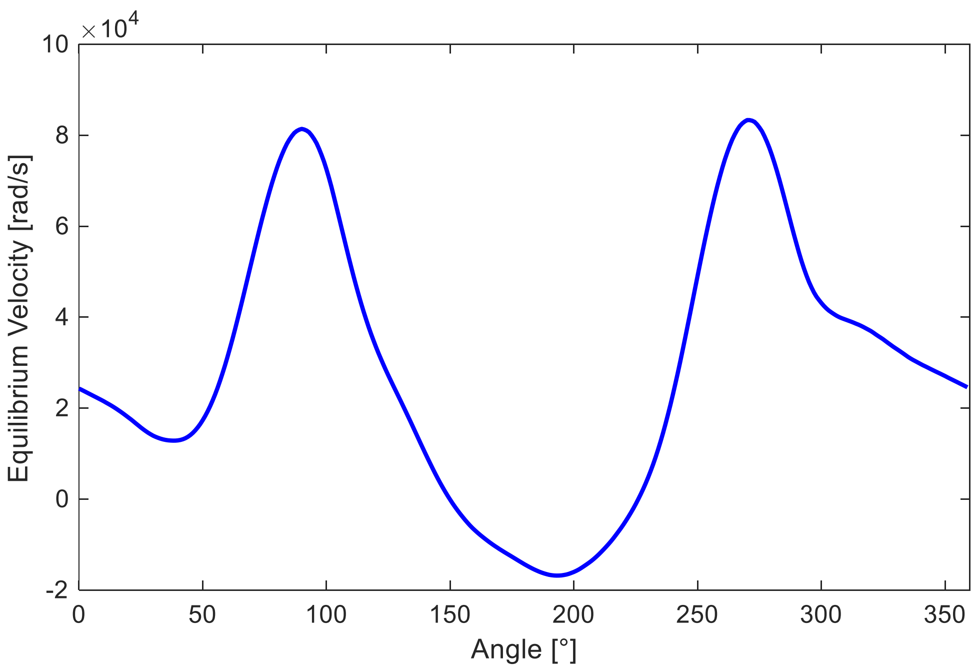

Figure 18. Wrap fiber equilibrium velocity as a function of angle.

The results of the one-dimensional model show good correlation to the air tangential velocity as calculated by the CFD. Peaks in the equilibrium velocity are seen around $90°$ and $270°$, in line with location of the air jets. The model also predicts a small region between $150°$ and $230°$ where the equilibrium velocity is negative. This again correlates well with the CFD results, as the tangential air velocity also becomes negative in this region. Going back to the physical geometry of the spinning chamber, the fiber induction zone is located near the middle of this interval, at $180°$. In this region where the fibers are introduced, a strong vertical component of air velocity exists, which interferes with the swirl in the spinning chamber. By placing the tangential air nozzles at a different position around the circumference of the spinning chamber, the impact of the fiber induction region can be reduced, increasing the mean equilibrium velocity.

While the one-dimensional is able to predict the velocity at which the wrap fibers experience zero torque due to aerodynamic drag, the physical meaning of the results is called into question, as the fiber can not accelerate or decelerate to these velocities instantaneously. Furthermore, this model would suggest that if the wrap fibers are introduced around $150°$, they would settle into a steady-state equilibrium at zero velocity. Many of the velocities predicted by this model also fall outside the range of rotational rates suggested by Krause and Nakahara, and they do not correspond to the results obtained from the geometric model. Despite this, taking the mean of all predicted fiber velocities yields an equilibrium velocity of $28500\,\frac{\text{rad}}{\text{s}}$, which is similar to the results discussed previously.

To include the effects of the fiber accelerating and decelerating, the two-dimensional model was developed. The results of the two-dimensional model are shown below for the same CFD data used in the one-dimensional model discussed previously.

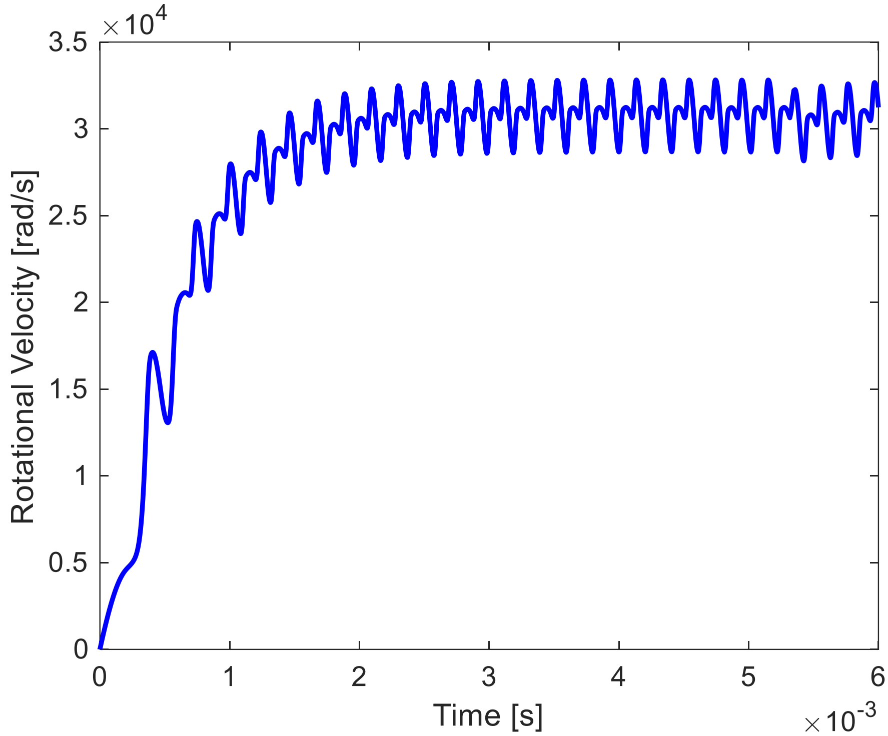

Figure 19. Wrap fiber velocity as a function of time using two-dimensional model.

With the two-dimensional model, the effects of the fiber's mass are evident, as it accelerates from rest before reaching a quasi-steady-state equilibrium. The periodic fluctuations in the wrap fiber's velocity correspond to the tangential location of the air jets and fiber inlet, confirmed in the figure below where the rotational velocity is plotted as a function of the fiber's angle.

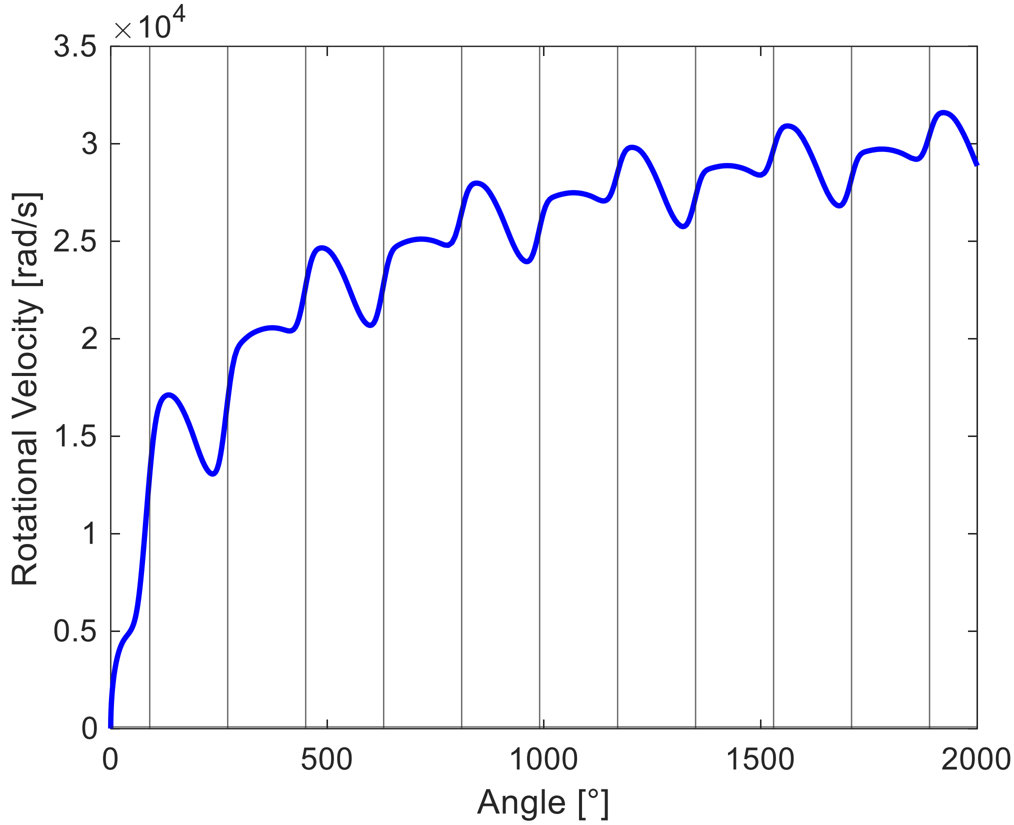

Figure 20. Wrap fiber velocity as a function of fiber angle.

Vertical lines are added to the plot at 90°, and every 180° thereafter to represent the fiber passing the location of the tangential air jets. As can be seen, the regions where the fiber is accelerating directly correspond to the location of the air jets.

The quasi-steady-state velocity of the wrap fiber was found by taking the mean velocity from time $t = 3$ ms to $t = 6$ ms. It was found to be $30900 \frac{\text{rad}}{\text{s}}$, once again similar to the previous predictions.

2.7.1 Variation in Wrap Plane Height

One of the parameters chosen for study was the effect of the wrap plane height on the fiber wrap speed. The initial wrap height, denoted by 0 μm above the spindle was chosen such that the fiber makes contact with the top of the spindle as it traverses the circumference of the yarn core.

It was thought that this would reduce the angular velocity of the wrap fiber as it travels through the boundary layer produced by the presence of the spindle. Four additional wrap plane heights were chosen for analysis.

The one-dimensional model produced the following plot of the equilibrium rotation rate of the fiber vs the angle of the fiber in the spinning chamber. As can be seen, the height of the wrap plane had a noticeable effect on the equilibrium velocity.

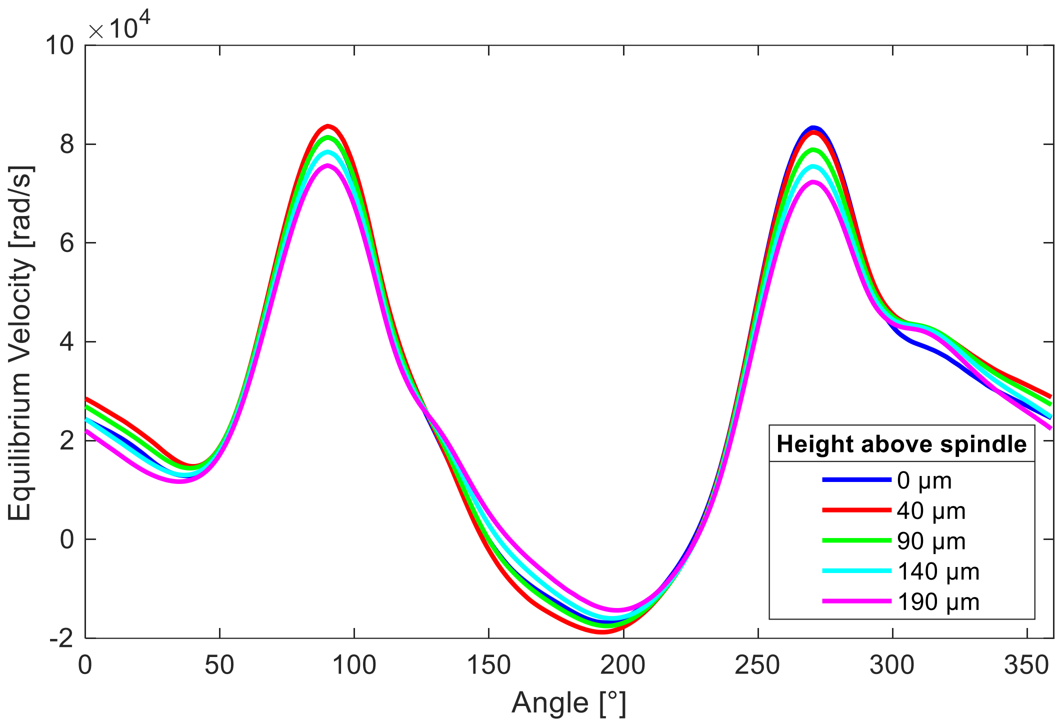

Figure 21. Wrap fiber equilibrium velocity as a function of angle for various heights.

The two-dimensional model produced the following plot of the fiber's angular velocity as a function of time.

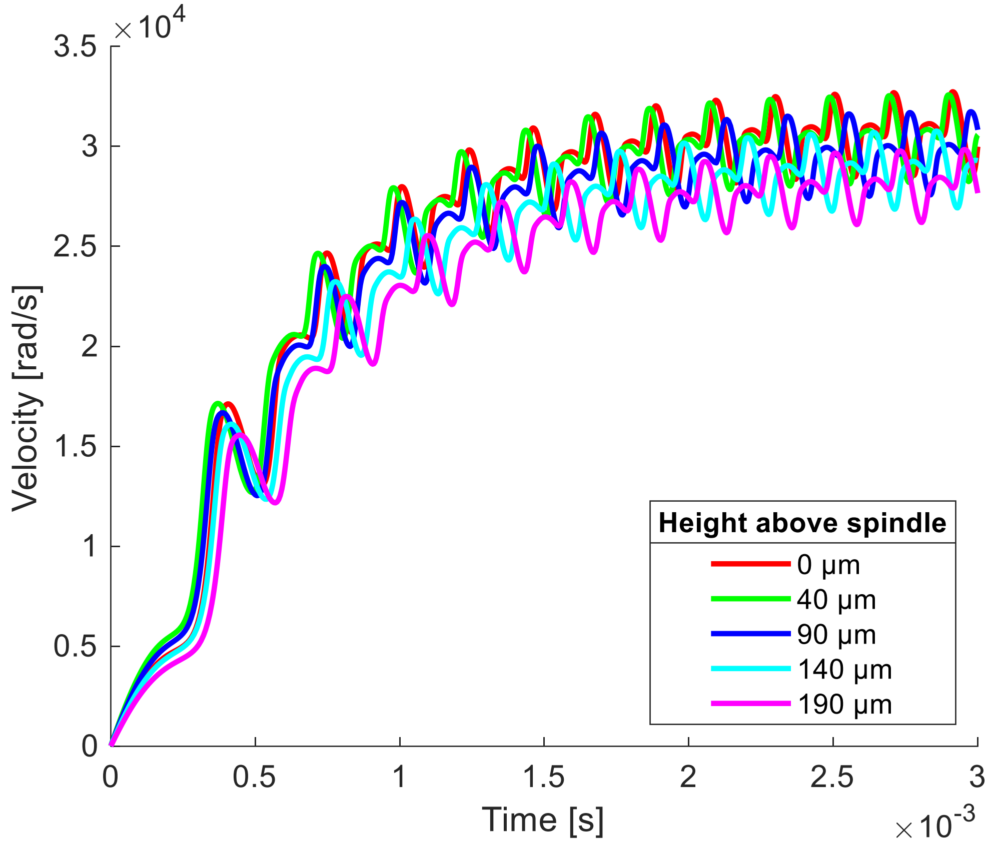

Figure 22. 2D fiber model sensitivity to wrap plane height.

Both models show that as the wrap plane travels up the *z*-axis, the fiber wrap velocity decreases. It can be concluded that the advantages of leaving the spindle's boundary layer do not outweigh the disadvantage of leaving the air jets' optimal height. The results are summarized in the table below.

Table 2. Wrap plane height effect on fiber velocity.

Wrap plane height	$\boldsymbol{z = 0\ \mu m}$	$\boldsymbol{z = 40\ \mu m}$	$\boldsymbol{z = 90\ \mu m}$	$\boldsymbol{z = 140\ \mu m}$	$\boldsymbol{z = 190\ \mu m}$
1D Model mean velocity	$28500\,\frac{\text{rad}}{\text{s}}$	$29425\,\frac{\text{rad}}{\text{s}}$	$28855\,\frac{\text{rad}}{\text{s}}$	$28044\,\frac{\text{rad}}{\text{s}}$	$27214\,\frac{\text{rad}}{\text{s}}$
2D Model quasi-steady-state velocity	$30866\,\frac{\text{rad}}{\text{s}}$	$30694\,\frac{\text{rad}}{\text{s}}$	$29978\,\frac{\text{rad}}{\text{s}}$	$29158\,\frac{\text{rad}}{\text{s}}$	$28365\,\frac{\text{rad}}{\text{s}}$

2.7.2 Variation in Fiber Drag Coefficient

As the resulting equation presented earlier for the drag coefficient of the fibers as a function of their Reynolds number was based on empirical data, concerns were raised over the applicability of the equation. Specifically, the surface roughness of the fibers may have been different to the test articles, varying the drag coefficient. Thus, simulations of the fiber motion were completed using different values for the drag coefficient, with the results being shown below. Data was taken from the nominal wrap height, $z = 0$ µm. The 1D model was not affected by variations in drag coefficients; the drag coefficient purely affects the fibers in a transient manner.

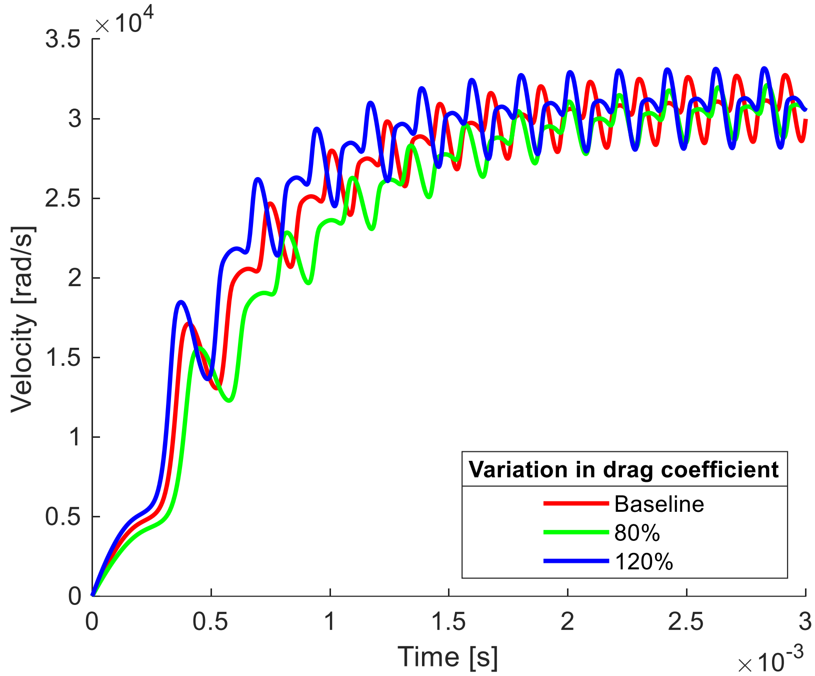

Figure 23. Fiber velocity as a function of time with varying drag coefficients.

Table 3. Drag coefficient effect on fiber velocity.

Drag coefficient variation	**Baseline C_d**	**$1.2\ C_d$**	**$0.8\ C_d$**
1D Model mean velocity	$28500\,\frac{\text{rad}}{\text{s}}$	$28500\,\frac{\text{rad}}{\text{s}}$	$28500\,\frac{\text{rad}}{\text{s}}$
2D Model quasi-steady-state velocity	$30866\,\frac{\text{rad}}{\text{s}}$	$30929\,\frac{\text{rad}}{\text{s}}$	$30919\,\frac{\text{rad}}{\text{s}}$

2.7.3 Sensitivity to Initial Conditions

As the two-dimensional fiber dynamic model is built around a differential equation of motion, it comes as no surprise that the solution exhibits some sensitivity to the initial conditions (ICs). When solving for the fiber's motion, the two initial conditions which require specification are the fiber's velocity, and the fiber's position. For the simulations presented above, these were set to $10\,\frac{\text{rad}}{\text{s}}$, and $0°$ arbitrarily, although as can be seen from the following results, aside from a region from $120°$ to $180°$, neither condition greatly influenced the fiber's motion. The slight differences in the fiber's quasi-steady-state velocity likely stem from the numerical solution, and for most purposes, the final velocity can be assumed to be independent of the initial conditions.

Table 4. Fiber quasi-steady-state velocity sensitivity to initial angle.

Initial condition	$\dot{\theta} = 0\,\frac{\text{rad}}{\text{s}}$ $\theta = 0$	$\dot{\theta} = 0\,\frac{\text{rad}}{\text{s}}$ $\theta = 60$	$\dot{\theta} = 0\,\frac{\text{rad}}{\text{s}}$ $\theta = 120$	$\dot{\theta} = 0\,\frac{\text{rad}}{\text{s}}$ $\theta = 180$	$\dot{\theta} = 0\,\frac{\text{rad}}{\text{s}}$ $\theta = 240$	$\dot{\theta} = 0\,\frac{\text{rad}}{\text{s}}$ $\theta = 300$
Quasi-steady-state velocity	$30900\,\frac{\text{rad}}{\text{s}}$	$30924\,\frac{\text{rad}}{\text{s}}$	$0\,\frac{\text{rad}}{\text{s}}$	$0\,\frac{\text{rad}}{\text{s}}$	$30912\,\frac{\text{rad}}{\text{s}}$	$30928\,\frac{\text{rad}}{\text{s}}$

Table 5. Fiber quasi-steady-state velocity sensitivity to initial velocity.

Initial condition	$\dot{\theta} = 0\,\frac{\text{rad}}{\text{s}}$ $\theta = 0°$	$\dot{\theta} = 10000\,\frac{\text{rad}}{\text{s}}$ $\theta = 0°$	$\dot{\theta} = 20000\,\frac{\text{rad}}{\text{s}}$ $\theta = 0°$	$\dot{\theta} = 30000\,\frac{\text{rad}}{\text{s}}$ $\theta = 0°$	$\dot{\theta} = 40000\,\frac{\text{rad}}{\text{s}}$ $\theta = 0°$	$\dot{\theta} = 50000\,\frac{\text{rad}}{\text{s}}$ $\theta = 0°$
Quasi-steady-state velocity	$30976\,\frac{\text{rad}}{\text{s}}$	$30906\,\frac{\text{rad}}{\text{s}}$	$30948\,\frac{\text{rad}}{\text{s}}$	$30980\,\frac{\text{rad}}{\text{s}}$	$30952\,\frac{\text{rad}}{\text{s}}$	$30926\,\frac{\text{rad}}{\text{s}}$

One condition which was briefly mentioned earlier was the location in the spinning chamber where the equilibrium velocity was zero. This would, in theory create some solutions where the fiber does not spin, and instead oscillates around this point. To test this, an initial condition of $0\,\frac{\text{rad}}{\text{s}}$ and $150°$ was used, producing the following results.

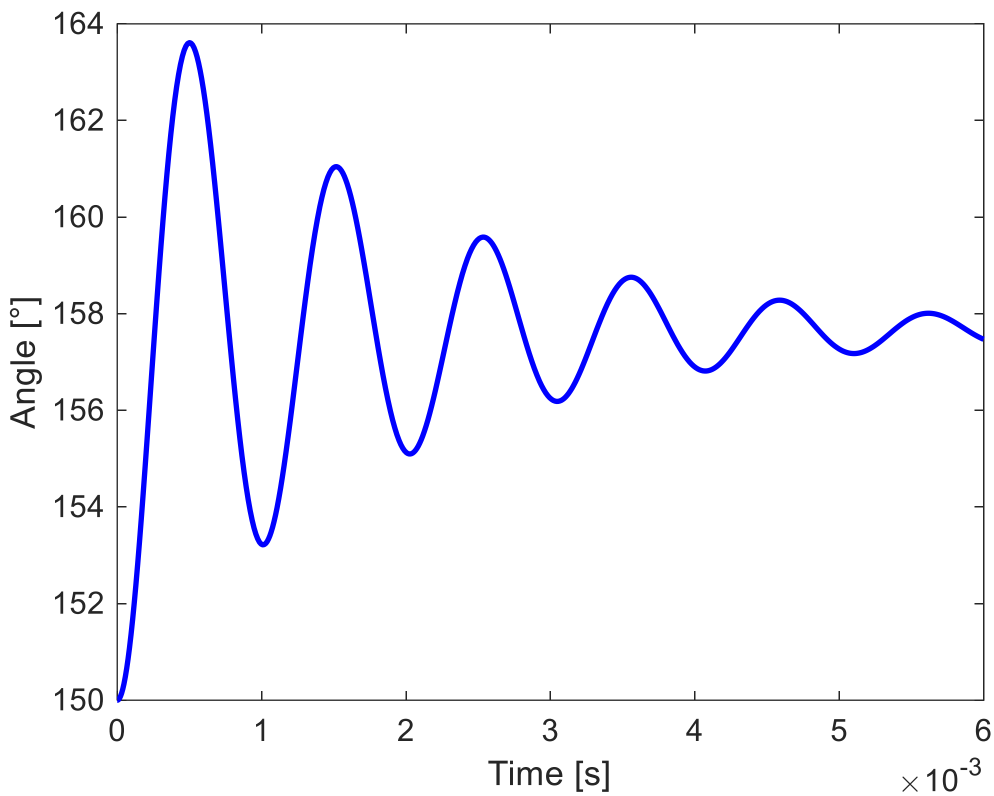

Figure 24. Fiber position as a function of time with 150° initial condition.

As can be seen, the results confirm this hypothesis, with the equilibrium angle occurring around 158°. Similar results were achieved using initial conditions of 120° and 180°. It is possible that this condition is present in the spinning chamber, although the stationary fiber would likely become part of the core fibers, or expelled with other fibers that do not become part of the final yarn.

2.7.4 Tensile Stress in the Fiber and Theoretical Maximum Production Rates

Due to the high rotational rates of the wrap fibers, they are subjected to large tensile stresses. The tension in the fiber can be described with the equation for the tension distribution in a uniform rod rotating about an axis perpendicular to its length. It is given by the following equation, with m_f representing the mass of the fiber, $\dot{\theta}$ representing the angular velocity, L_f

representing the length of the fiber, and r representing the radial position at which the tension is calculated.

$$F_t(r) = \frac{m_f \dot{\theta}^2}{2L_f}(L_f^2 - r^2)$$

Of note is that the tension distribution in the fiber is not uniform, the stationary end of the fiber experiences the most, while the tension in the free end is zero. The parameter of more interest is the stress developed in the fiber as a result of this tension. The stress in the fiber can be defined with the following equation.

$$\sigma_t = \frac{F_t}{A_{circ}} = \frac{m_f \dot{\theta}^2}{\frac{\pi}{4} D_f^2 \cdot 2L_f}(L_f^2 - r^2) = \frac{\rho_f \dot{\theta}^2}{2}(L_f^2 - r^2)$$

The figure below depicts the tensile stress distribution in a 2mm acrylic fiber rotating at $28000\ \frac{\text{rad}}{\text{s}}$. The resulting stress distribution matches predictions, with a maximum value of 1.8 MPa at the fixed end, gradually reducing to zero at the free end.

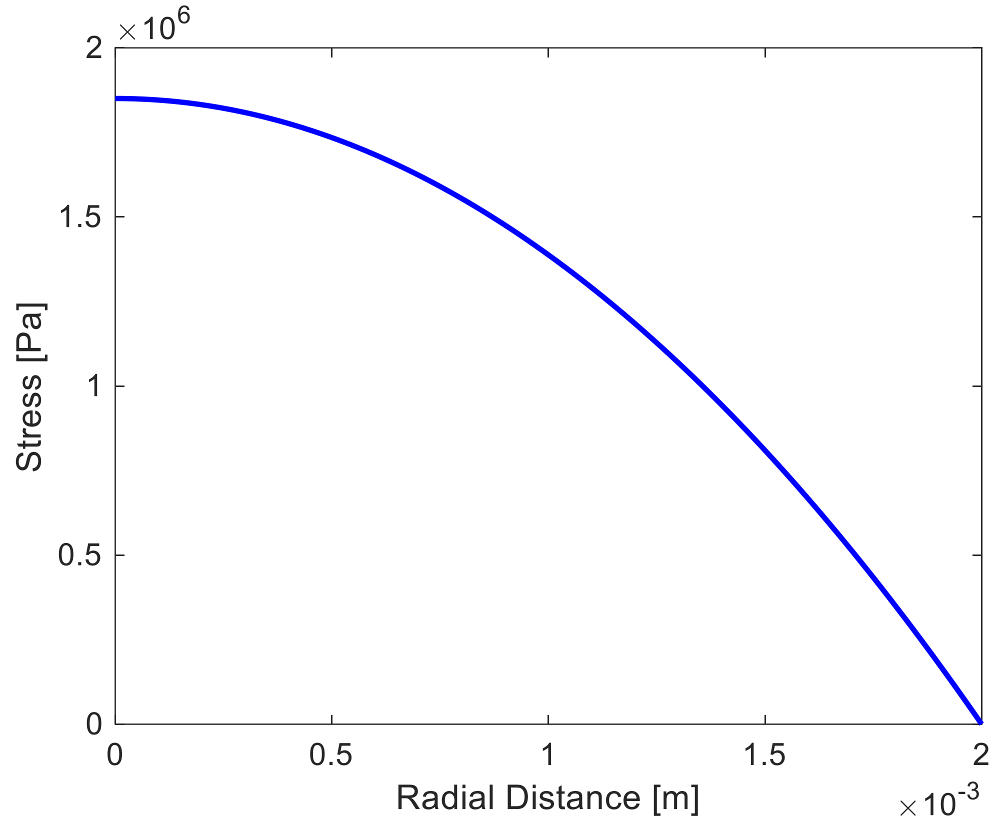

Figure 25. Tensile stress distribution in spinning wrap fiber.

For a fiber in pure tension, it can be assumed that the maximum stress it can endure without failure is equal to the ultimate tensile strength (UTS) of the material, a physical property which has been well-characterized in the past. The implication of this is that for a given fiber length and density, there is a maximum rotational velocity at which the fibers can spin before the tensile stress exceeds the UTS of the material, which would cause the fiber to tear apart before successfully constraining the core fibers. For a $2\ \mathrm{mm}$ acrylic fiber with a UTS of 63 MPa, this limit is reached at approximately $163000\,\frac{\mathrm{rad}}{\mathrm{s}}$. The same is true for all fibers, with higher strengths leading to a higher theoretical maximum production rate. Assuming a yarn diameter of $120\ \mu\mathrm{m}$ and wrap angle of $12°$, the geometric model correlates this angular speed to a production rate of $46\,\frac{\mathrm{m}}{\mathrm{s}}$, or $2760\,\frac{\mathrm{m}}{\mathrm{min}}$. This rate, the proposed Leite de Moraes (LDM) limit, effectively caps the production rate of yarn, with current production rates approaching 20% of this limit for acrylic fibers. This limit can be mitigated by increasing the wrap angle of the yarn, although this may have an effect on other properties of the yarn, making reducing the wrap angle undesirable. Materials with low density and high UTS will also have a greater maximum theoretical production rate.

2.8 Experimental Measurements

To validate the computational and analytical results, modifications were made to the Savio Lybra air jet spinner. These modifications include the installation of mass flow meters, static pressure taps, and the addition of a glass window to allow for optical access to the spinning chamber. For testing, a stand was assembled which holds the nozzle and associated components such as pressure regulators and valves.

2.8.1 Design of Modified Spinning Chamber

Several design revisions were compared for overall optical access. The first design relied on the ability to 3D print with transparent resin. It was thought that by replacing parts of the nozzle with transparent alternatives, optical access to the spinning chamber would be possible. Upon testing, the 3D printed components caused too many distortions to the transmitted light, making optical access to the chamber unfeasible.

The second revision instead relied on modifications to the air delivery system of the spinning chamber to cut away parts of the nozzle obstructing the view. Additionally, part of the spinning chamber was cut away, with a quartz window being installed in its place. This design was ultimately successful in allowing optical access to the spinning chamber, and was selected for use in a measurement campaign.

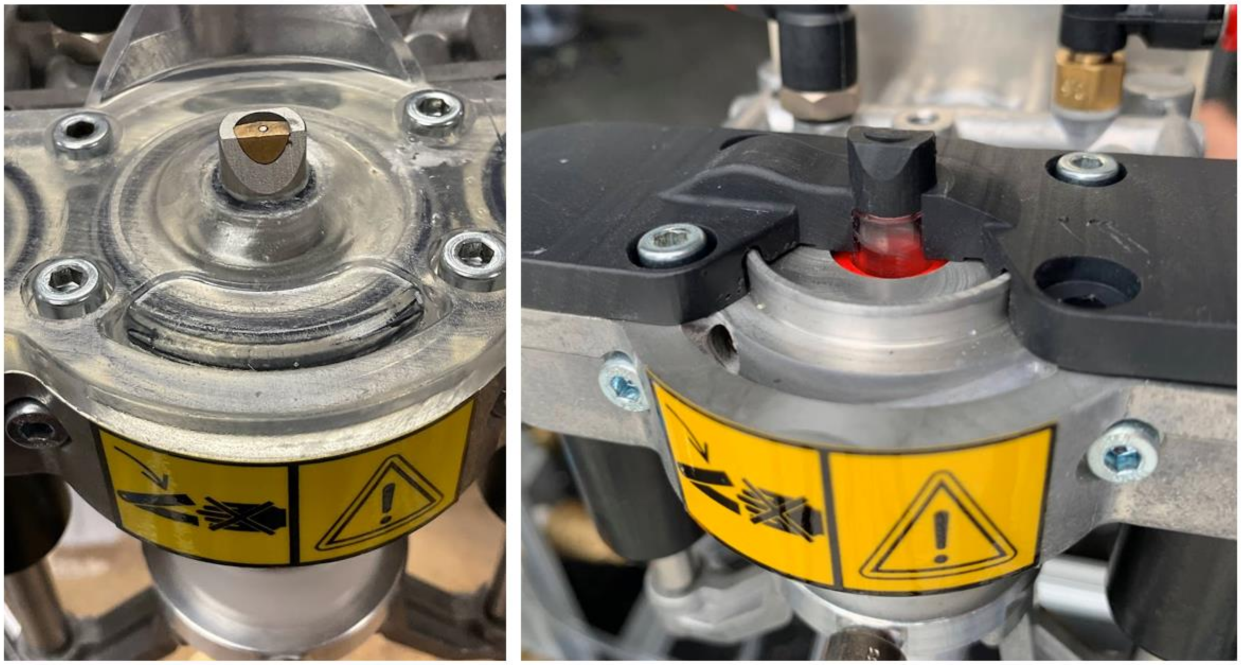

Figure 26. Nozzles modified for optical access. Left: Transparent 3D prints. Right: Glass window.

2.8.2 Images and Measurements of Spinning Process

To capture the spinning process, the modified Savio Lybra nozzle was installed on the respective machine, and a Photron FASTCAM NOVA R5-4K high speed camera was used to capture the production process at framerates up to 40000 FPS. An image of the modified nozzle installed on the spinning machine, with camera lens visible on the right is shown below.

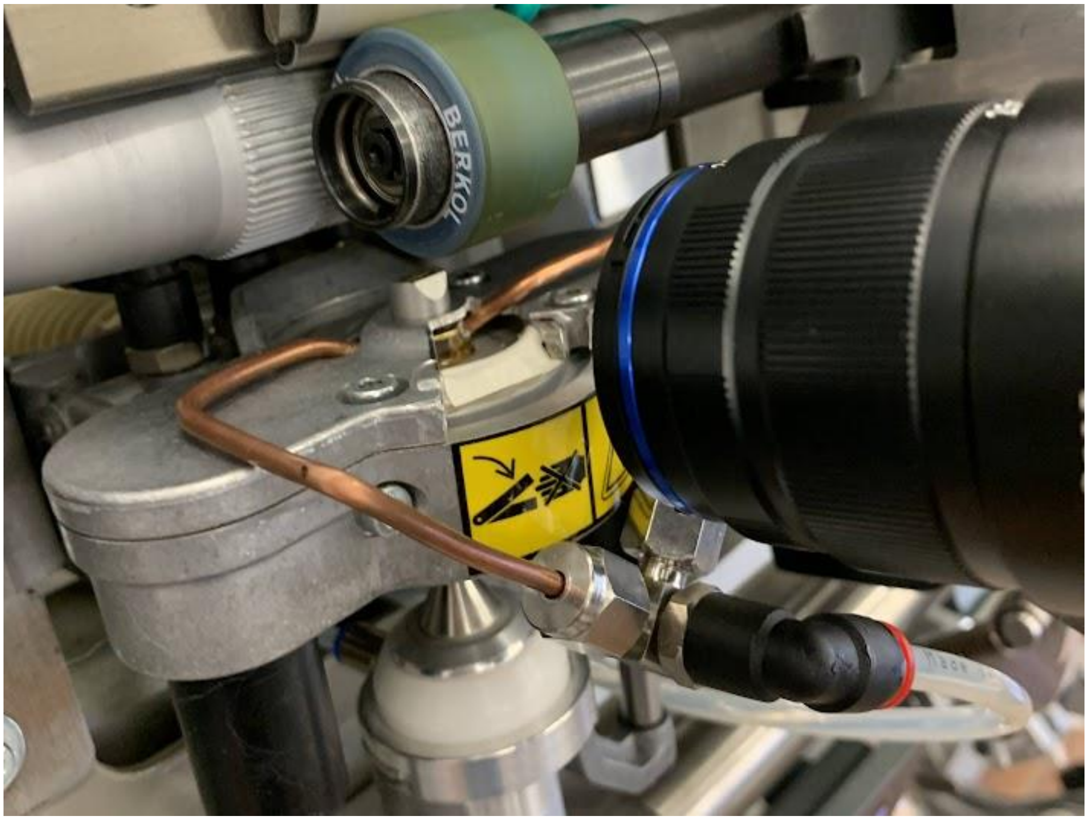

Figure 27. Modified Lybra nozzle with cutout and glass window for optical access.

The following image shows a frame captured by the FASTCAM NOVA at 8000 FPS using a 125 μs exposure time. Other tests traded the spatial resolution for temporal resolution, achieving framerates of up to 40000 FPS and exposure times of 25 μs.

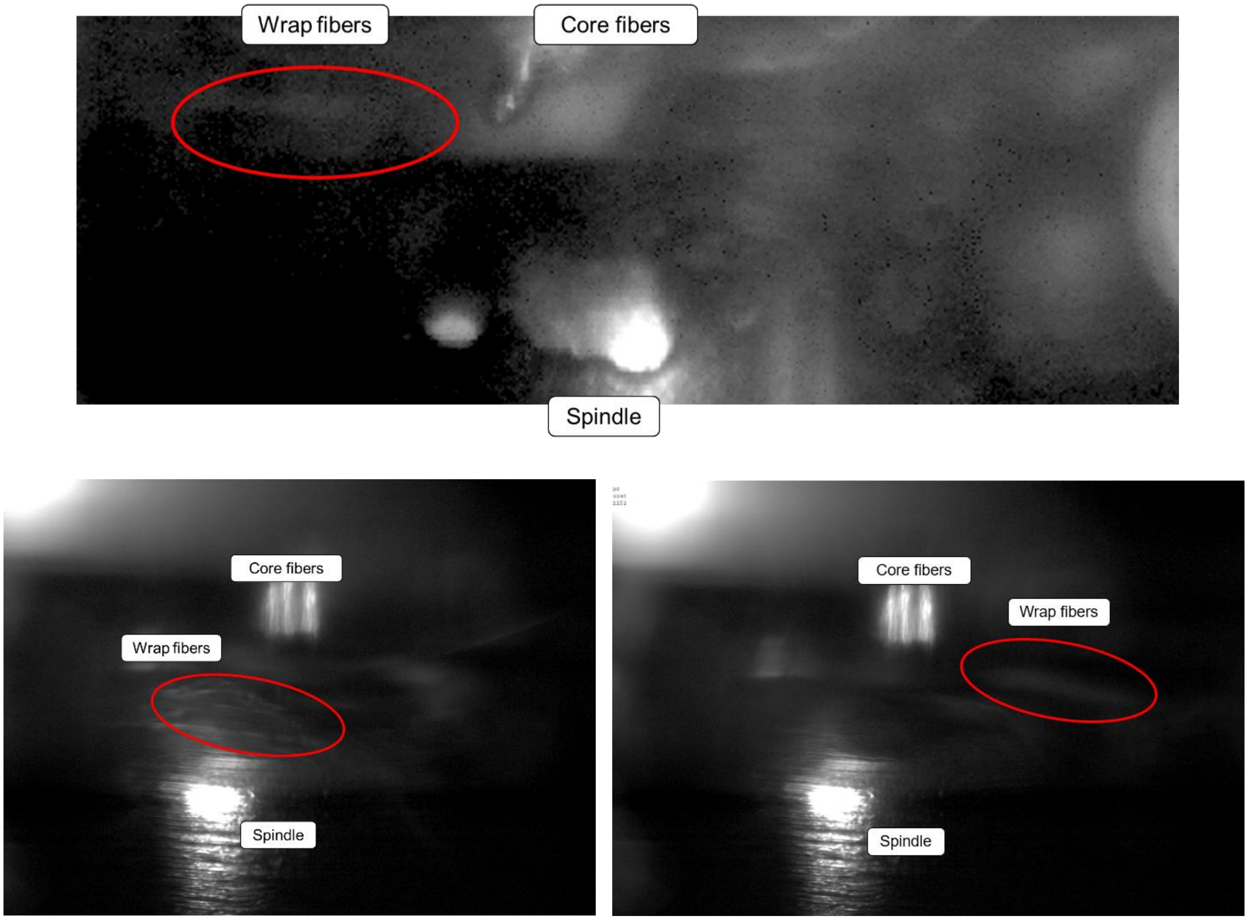

Figure 28. Images of spinning chamber and wrap fibers taken from high speed video.

Despite the modifications made to the spinning chamber, the machine was able to successfully produce yarn using acrylic and cotton fibers at a production rate of $350\,\frac{\mathrm{m}}{\mathrm{min}}$. The primary challenge which arose from capturing the high speed video was adequate lighting. The small size of the spinning chamber coupled with the short exposure time made it difficult to capture process with clear definition. By comparing the location of the wrap fibers between frames of the recorded videos, estimates for the angular distance traveled by the wrap fibers were obtained. Multiple series of frames were analyzed, and the angular velocity of the fibers was determined to be approximately $28000\,\frac{\mathrm{rad}}{\mathrm{s}}$, within the range suggested by Krause and Nakahara and similar to the results obtained from the geometric, 1D and 2D dynamic models.

3 Bladeless Turbine

3.1 Introduction

The most commonly discussed bladeless turbine is the one patented by Nicola Tesla in the early 1900s, which is a radial design using a series of flat disks closely spaced, using the viscous effects of a fluid entering the gaps in the tangential direction to generate torque [37]. Previous studies have aimed to examine the effects of adding a supersonic nozzle to the inlet of a Tesla turbine, concluding that the adequate design and implementation can lead to increased power production [38].

A supersonic axial bladeless turbine design was first proposed by Vinha et. al. in 2016 [39]. This design relies on a tangential component of the fluid inlet velocity to develop torque through viscous effects. This design showed a reduction in total pressure loss, and an optimum RPM for power extraction. Expanding on this design, Braun et. al. proposed adding a wavy surface geometry to the turbine in 2020 [5]. The wavy surface geometry is used to induce shock waves and expansion fans, thereby capturing pressure differentials to generate torque in addition to the viscous effects explored previously.

For a calorically perfect gas and assuming no heat transfer, the work extraction of a turbine can be related to the change in total temperature from the inlet to the outlet. With $\dot{W}$ representing the rate of energy output, $\dot{m}$ representing the mass flow rate of the gas, c_p representing the specific heat of the gas at constant pressure, and ΔT_0 representing the change in total temperature across the turbine, this can be represented through the following equation:

$$\dot{W} = \dot{m} c_p \Delta T_0$$

Work output can also be calculated as the product of torque τ and angular velocity ω. This definition is not affected by real gas effects, and is not sensitive to numerical diffusion present in

CFD simulations, making it the preferred choice for estimating the turbine's power output in this study. The equation is presented below.

$$\dot{W} = \tau\omega$$

3.2 Simplified One-dimensional Model and Operational Principle

As previously mentioned, the wavy bladeless turbine uses its wavy surface to induce a series of shock waves and expansion fans to generate strong pressure gradients, with a simplified geometry being shown below. All angled surfaces are placed 10° from the horizontal, implying that the oblique shock waves from location 1 to location 2 and location 5 to location 6 result in a flow turning angle of 10°, while the oblique shock wave from location 3 to location 4 results in a turning angle of 20°. Both expansion fans result in a flow turning angle of 20°.

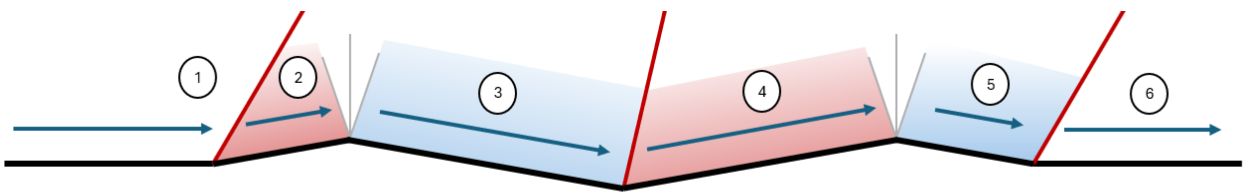

Figure 29. Simplified schematic of bladeless turbine shock wave and expansion fan formation.

Using the one-dimensional flow equations for supersonic flow including oblique shock relations and Prandtl-Meyer relations, thermodynamic properties including static pressures can be calculated at each location. The results of the calculations are shown in the table below, assuming a uniform inflow at Ma = 1.6, $P_s = 1$ bar.

Table 6. Mach number, static and total pressure across simplified cylindrical turbine.

	Location 1	**Location 2**	**Location 3**	**Location 4**	**Location 5**	**Location 6**
Mach number	1.6	1.24	1.93	1.12	1.84	1.49
Static pressure	1 bar	1.64 bar	0.59 bar	1.68 bar	0.61 bar	1.01 bar
Total pressure	4.25 bar	4.20 bar	4.20 bar	3.75 bar	3.75 bar	3.70 bar

As can be seen in the figure and from the results of the calculations, regions shaded in red represent a static pressure greater than the inlet, while regions shaded in blue represent a static pressure less than the inlet. This would be of little use in the two-dimensional case presented above, however by rotating this geometry around a central axis in a helical fashion, the pressure differential across the angled faces would generate torque. A simplified 3D rendering of such a geometry is shown below.

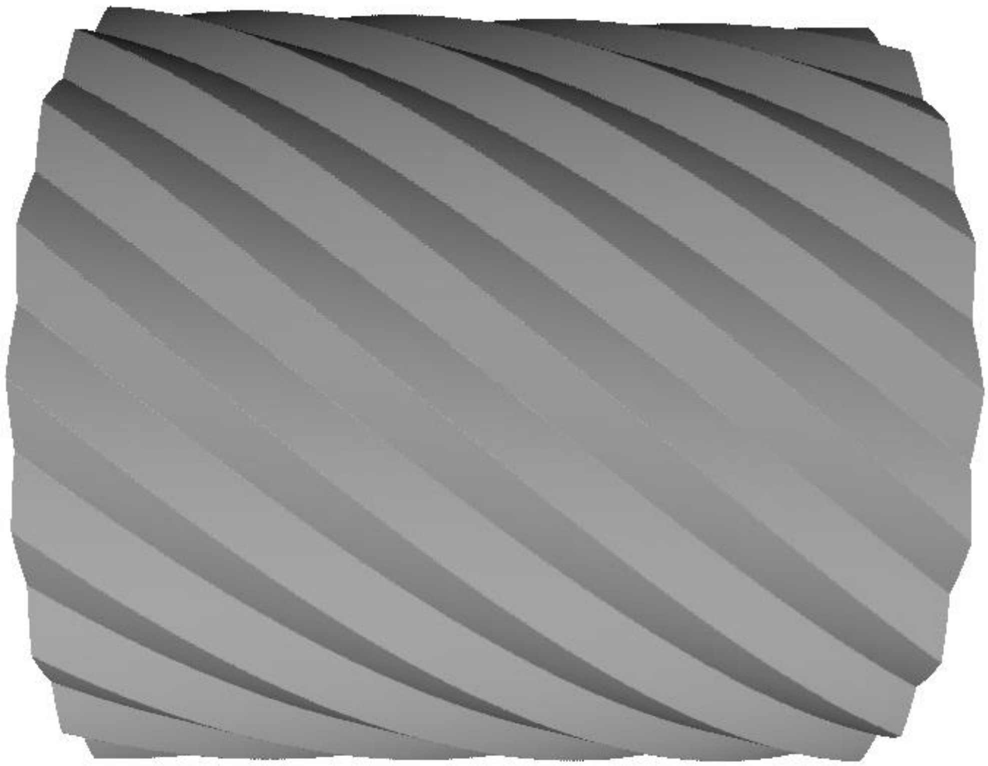

Figure 30. Simplified wavy turbine geometry.

It is hypothesized that the primary method of power generation from the bladeless turbine comes from inviscid, or pressure-based effects due to the rapid acceleration and deceleration of the flow through the shock waves and expansion fans. Skin friction along the outer surface of the turbine is not expected to significantly contribute to the total torque production.

3.3 Modifications for Experimental Testing

The limiting factor preventing the tests of the bladeless turbine geometry proposed by Braun et. al. was the lack of access to a suitable test facility. A facility suitable for testing the bladeless turbine would require an annular supersonic flow passage capable of mass flow rates of $4.18\,\frac{\mathrm{kg}}{\mathrm{s}}$, in addition to being able to dissipate the predicted 70 kW of mechanical power production.

To make testing the bladeless turbine more feasible, two proposed modifications were studied. The first involved resizing the turbine, using a non-dimensional study to predict the rotational rates and power output. The second involved modifying the shape of the turbine while also reducing the size. The proposed conical shape would eliminate the need for an annular supersonic passage, and instead a simpler free-jet facility could be used.

A dynamometer is a device which measures and absorbs the power output of a device under test. For the proposed testing of the bladeless turbine, three approaches were considered to serve as the basis for a dynamometer.

The first approach involved coupling the turbine to a compressor wheel of an automotive turbocharger, which would then act as an air-brake dynamometer. This concept has been proven, and is currently used in the gas turbine industry to test engines of up to 2.2 MW at rotational rates of 20000 RPM, demonstrating its adaptability to be used at different power scales [40]. By varying the backpressure or mass flow rate through the compressor, the power extraction from the turbine could be changed, and a turbine map could be created. Challenges with this approach involved uncertainty around the compressor. While a compressor map was provided by the manufacturer, the instrumentation and data acquisition system required to accurately measure the fluid properties at the inlet and outlet of the compressor would require extensive testing and calibration before the turbine's power output could be calculated with a reasonable degree of uncertainty.

The second approach considered the use of an electric motor to act as a generator, thereby absorbing the mechanical power produced by the turbine and converting it into electrical power. The electrical power could then be dissipated through a series of braking resistors, which would ultimately convert the power into heat. This concept has also been tested, with Sasaki proposing a design which operates at up to 100000 RPM, absorbing over 15 kW [41]. The instrumentation for this approach would be simplified when compared to the first, as voltage, current, and resistance are all quantities that can be measured quickly, and with a great degree of accuracy. By knowing the efficiency curve of the motor, these quantities can be converted back to provide an estimate for mechanical power. Finally, a torque sensor could be easily integrated into the mechanical design, and thus a redundant power measurement could be obtained.

The final approach considered for measuring the power production of the bladeless turbine involved coupling the turbine to a flywheel to act as rotational inertia. Through Newton's second law for rotating bodies ($\tau = I\ddot{\theta}$), the torque acting on the flywheel can be calculated if the rotational inertia and angular acceleration are known. The angular velocity of the flywheel can be easily calculated through taking the derivative of its velocity with respect to time, and the rotational inertia can be easily calculated using the physical properties of the flywheel including the size, shape, and mass. By measuring the turbine's rotational inertia using a constant torque, Yang et. al. were able to measure the power of a radial bladeless turbine, commonly known as a Tesla turbine, using this technique [42]. One of the challenges associated with this approach is that steady-state testing is not possible as the flywheel's velocity must vary with respect to time for torque to be absorbed.

3.3.1 Non-Dimensional Sizing

To estimate the effects of changing the turbine diameter on the power output and rotational rate, non-dimensional sizing study was performed. To do so, the Buchingham-Pi theorem was applied to a generalized turbomachine to yield the following equation as presented in [43]:

$$\frac{P_{02}}{P_{01}}, \frac{\dot{W}}{\rho_{01} N^3 D^5}, \eta, \text{etc.} = f\left(\frac{ND}{\sqrt{\gamma R T_{01}}}, \frac{\dot{m}\sqrt{T_{01}}}{P_{01}}\sqrt{\frac{R}{\gamma}}\frac{1}{D^2}, \mathrm{Re}, \gamma\right)$$

For the same working fluid, constants such as γ and R can be removed from the equation, yielding the following:

$$\frac{P_{02}}{P_{01}}, \frac{\dot{W}}{\rho_{01} N^3 D^5}, \eta, \text{etc.} = f\left(\frac{ND}{\sqrt{T_{01}}}, \frac{\dot{m}\sqrt{T_{01}}}{P_{01} D^2}, \text{Re}\right)$$

The proposed scaled bladeless turbine would use the same geometry of the one analyzed by Braun et. al., and operate at the same efficiency point. Furthermore, Reynolds effects can likely be ignored due to the turbulent regime in which the bladeless turbine operates, and the low variation of skin friction with Reynolds number in the turbulent regime. For these reasons, the change in flow enthalpy Δh_0 across the original turbine and the scaled turbine can be assumed to be constant. From the conservation of energy, the change in flow enthalpy across the turbine can be related to the power output using the mass flow rate as seen in the following equation:

$$\dot{W} = \Delta h_0 \dot{m}$$

Thus, the variation in mass flow rate will directly dictate the power output of the scaled turbine. By equating the flow coefficients $\frac{\dot{m}\sqrt{T_{01}}}{P_{01} D^2}$ between both turbines, a relationship between the power extraction and turbine diameter can be created. The total temperature and pressure (T_{01}, P_{01}) were assumed equal for both turbines. After substituting and simplifying, the final equation for the power output as a function of turbine diameter was developed:

$$\frac{\dot{W}_{scaled}}{\dot{W}_{Braun}} = \left(\frac{D_{scaled}}{D_{Braun}}\right)^2$$

To expand this, the speed coefficients $\frac{ND}{\sqrt{T_{01}}}$ were also equated between the scaled and the original to predict the rotational velocity of the subscale model. Again, the total temperature was assumed equal between both, yielding the following:

$$\frac{N_{Braun}}{N_{scaled}} = \frac{D_{scaled}}{D_{Braun}}$$

Using the diameter, rotational speed, and predicted power output published by Bruan et. al., the scale turbine diameter can be varied to produce the following graphs.

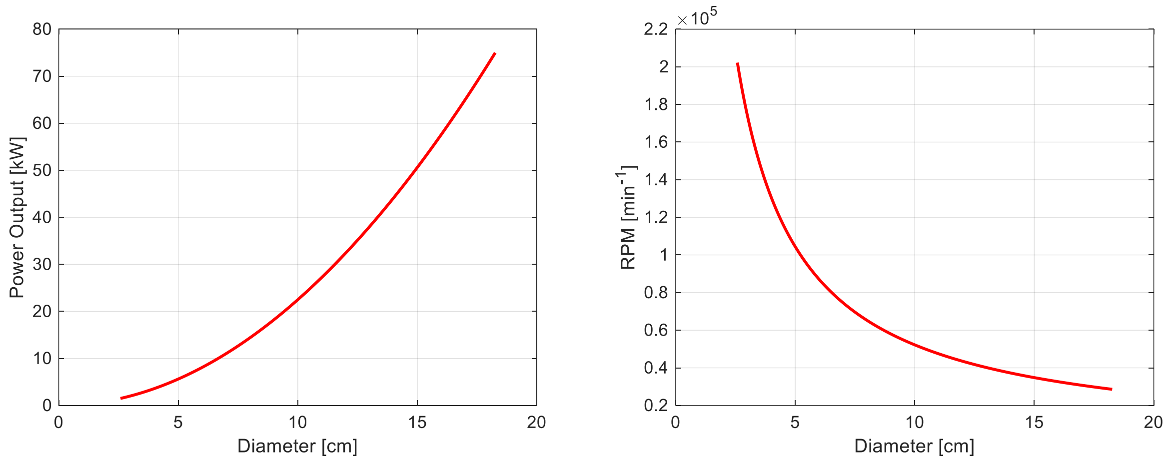

Figure 31. Power output and rotational velocity as a function of turbine diameter.

3.3.2 Novel Conical Turbine

Another aspect of the bladeless turbine that would make testing challenging is the need for an annular supersonic passage. To eliminate this need, it was at first proposed to add a nose cone along the axis of the turbine to redirect the flow around it. While this may have been effective if the turbine operated in the subsonic regime, a shock wave would have formed at the tip of the cone during the turbine's supersonic operation. This shock wave would redirect the flow, however the interaction between the shock wave and expansion fan caused by the cone were deemed undesirable as they would likely reduce the turbine's power output as compared to the nominal annular case. Instead, it was proposed to take advantage of the shock wave generated at the tip by applying the wavy surface to the cone itself. By doing so the bladeless turbine becomes more suitable for use in free-stream flow conditions, such as the proposed free-jet test facility. A simplified diagram of the turbine shock waves and expansion fans, is shown below. A cone angle of $\beta = 18.4°$ is used, with ramp angles of $\pm 5°$ to represent the wavy surface.

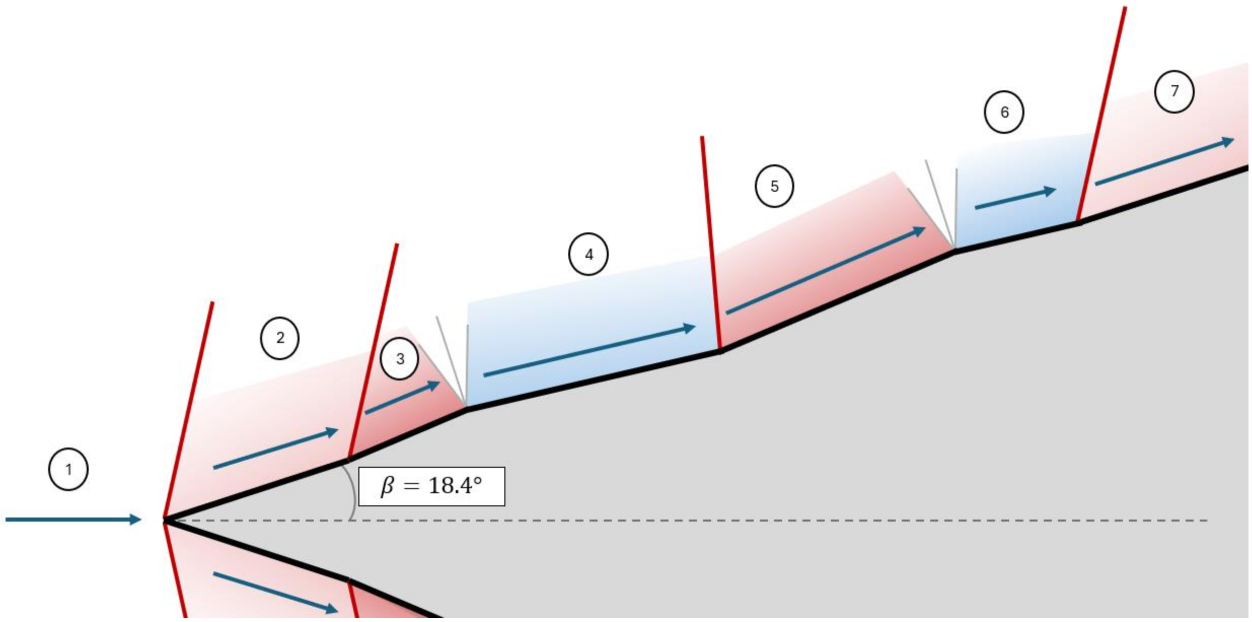

Figure 32. Conical bladeless turbine simplified diagram.

Once again, using the one-dimensional equations for supersonic flow, the Mach numbers and pressures can be calculated at each location. Of note is that the shockwave from location 1 to location 2 is not oblique, but rather conical due to the 3D nature of the turbine. A uniform inflow at $\mathrm{Ma} = 1.6$, $P_s = 1$ bar was used.

Table 7. Mach number, static and total pressure across simplified conical turbine.

	Location 1	**Location 2**	**Location 3**	**Location 4**	**Location 5**	**Location 6**	**Location 7**
Mach number	1.6	1.28	1.06	1.46	1.05	1.45	1.27
Static pressure	1 bar	1.3 bar	1.72 bar	1.01bar	1.72 bar	1.01 bar	1.29 bar
Total pressure	4.25 bar	4.24 bar	4.23 bar	4.23 bar	4.17 bar	4.17 bar	4.16 bar

To achieve a constant helix angle along the axial length of the turbine, a logarithmic function was used to define the twist angle as a result of the variable radius. An image of the conical turbine is shown in later sections, along with discussions and details about the geometry generation.

3.4 Computational Simulations of the Bladeless Turbine

To more effectively contribute to the development of the bladeless turbine, the parameters and solution techniques used in [5] were followed wherever possible to maintain continuity. This included using the same software solutions, Numeca HEXPRESS for meshing, and MetaComp iCFD++ for domain decomposition, solving, and post-processing of the results in addition to MathWorks MATLAB and TecPlot360.

3.4.1 Domain Generation

To generate the CAD model of the bladeless turbine, a MATLAB script was created to generate a series of coordinates along the outer wall of the turbine surface. MATLAB was used to parameterize the generation of the curve, with the parameter t taking values from $t = 0$ to $t = 2\pi$.

Variables A, f, and B represent the turbine's wave amplitude as a percentage of the mean radius, number of waves, and mean radius respectively. The parametric equations of the curve take the following form.

$$R(t) = (A \cdot \cos(f \cdot t) + 1) \cdot B$$

$$\theta(t) = A \cdot \cos(f \cdot t) + t$$

A plot of a turbine surface with $A = 0.02$, $f = 20$, and $B = 5$ is shown below for reference.

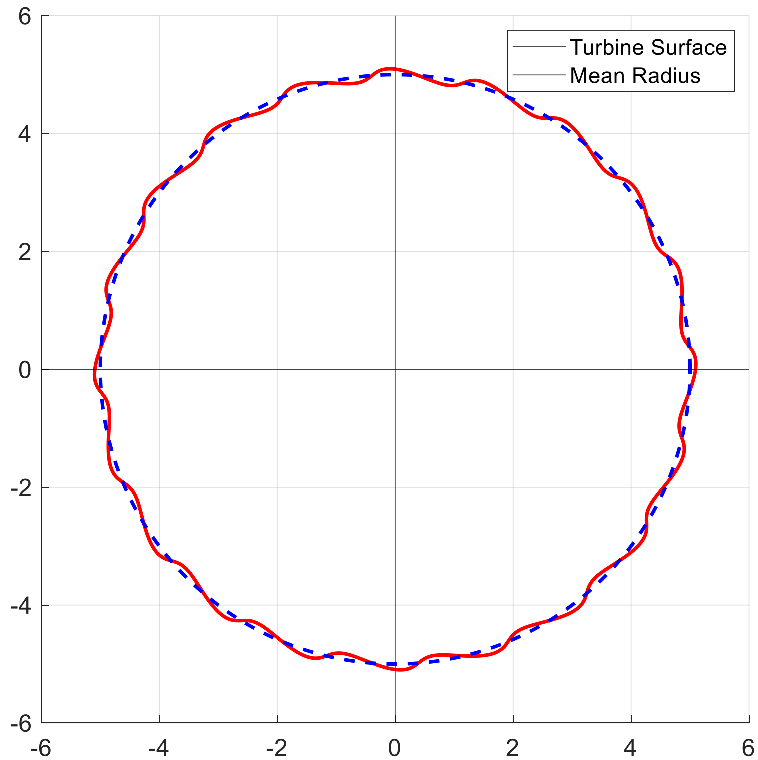

Figure 33. 2D plot of turbine surface and mean radius.

With the coordinates of the curve exported, they could then be brought into SolidWorks using the "Curve through XYZ points" tool. After defining helixes which pass through the curve and whose height defined the axial length of the turbine, the outer surface could then be lofted using the helices as guide rails to create the CAD model of the turbine.

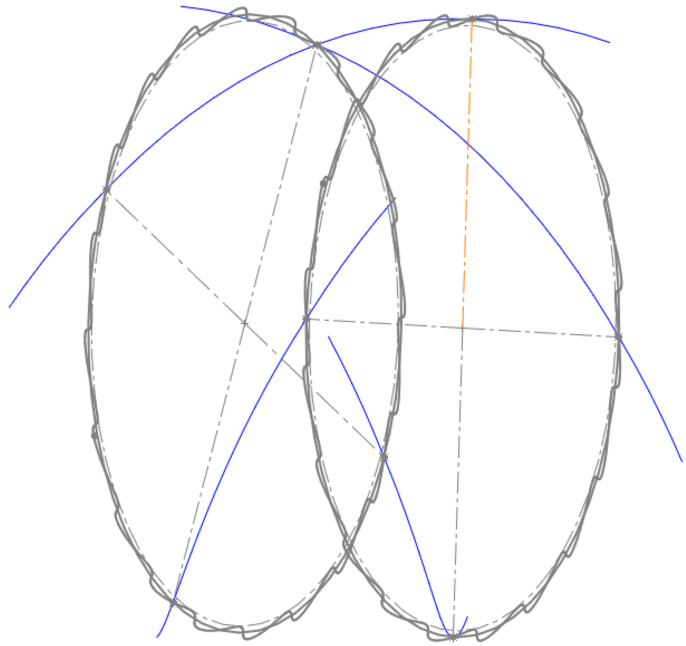

Figure 34. Parametrized turbine curves with four helices used as loft guide curves.

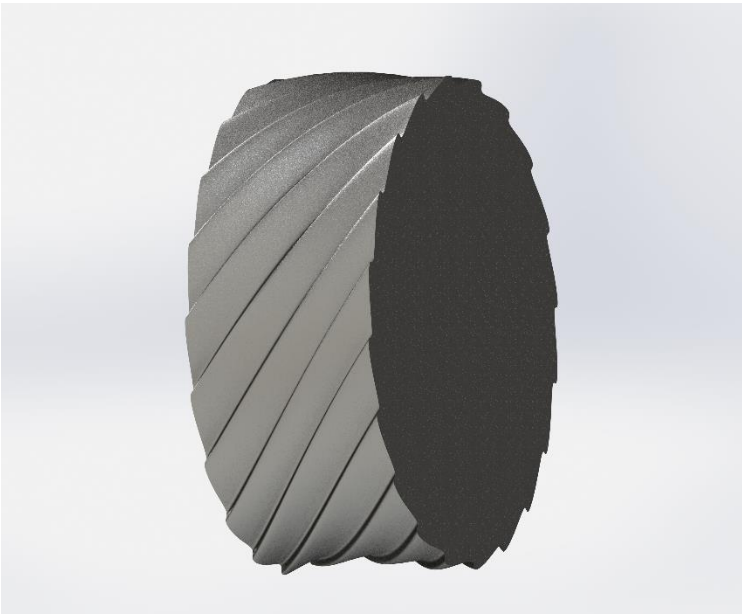

Figure 35. SolidWorks rendering of bladeless turbine geometry.

While this technique produced adequate results, the numerous steps involved were error-prone, time-consuming, and provided little flexibility to modify the shape of the turbine.

To simplify the generation of the bladeless turbine, the original MATLAB script was updated to extend the turbine in the axial direction. This was done by creating a number of points along the axial length of the turbine, and re-calculating the desired outer surface geometry at these axial locations. By doing this, parameters such as the wave amplitude, helix angle and mean radius can all be varied as functions of axial length, something not possible in SolidWorks. Varying the wave amplitude produces a smooth transition between the annular flow to the wavy surface, while varying the radius creates the conical geometry discussed previously.

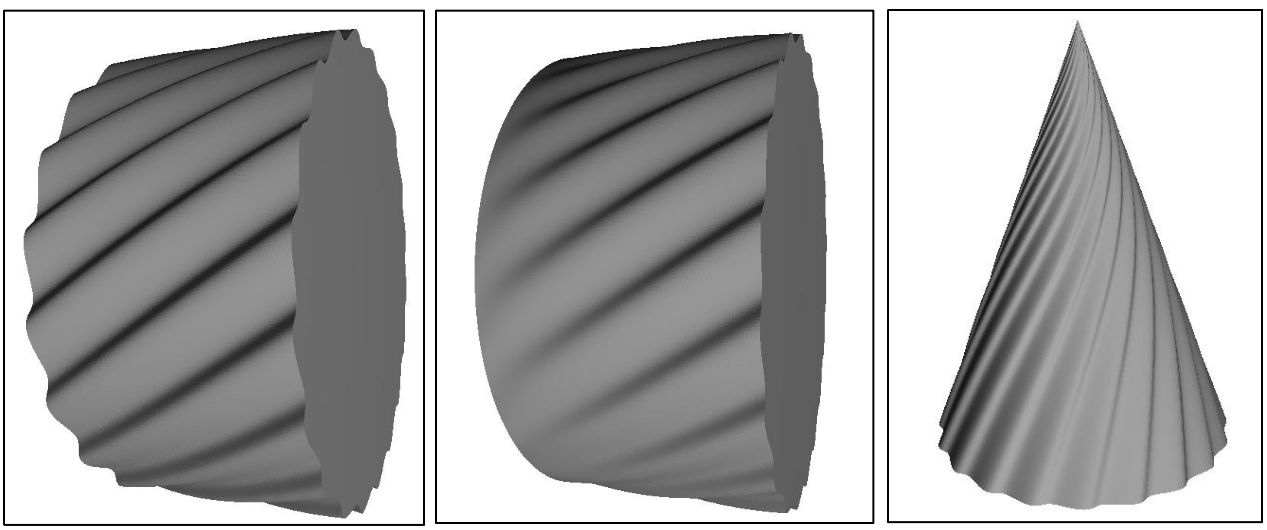

Figure 36. Bladeless turbine geometries generated using MATLAB. A) Baseline geometry. B) Variation in wave amplitude. C) Conical.

To export the geometry from MATLAB, the function *stlwrite* was used [44]. The resulting .stl file can then be brought into SolidWorks for further manipulation, such as adding a shaft or housing to the turbine. The .stl files generated by the MATLAB script represent the solid domain of the turbine. Before CFD simulations of the turbine can be performed, a fluidic domain must be generated. While this is possible in HEXPRESS, the MATLAB script was instead modified. Due to the rotational symmetry of the turbine, an angular sector of the turbine could be modeled instead of the full geometry. This reduces the total cell count of the fluid domain, and by specifying periodic boundary conditions to the CFD solver, the accuracy of the solution is unchanged. The procedure for generating the fluid domain in MATLAB is described in the following diagram.

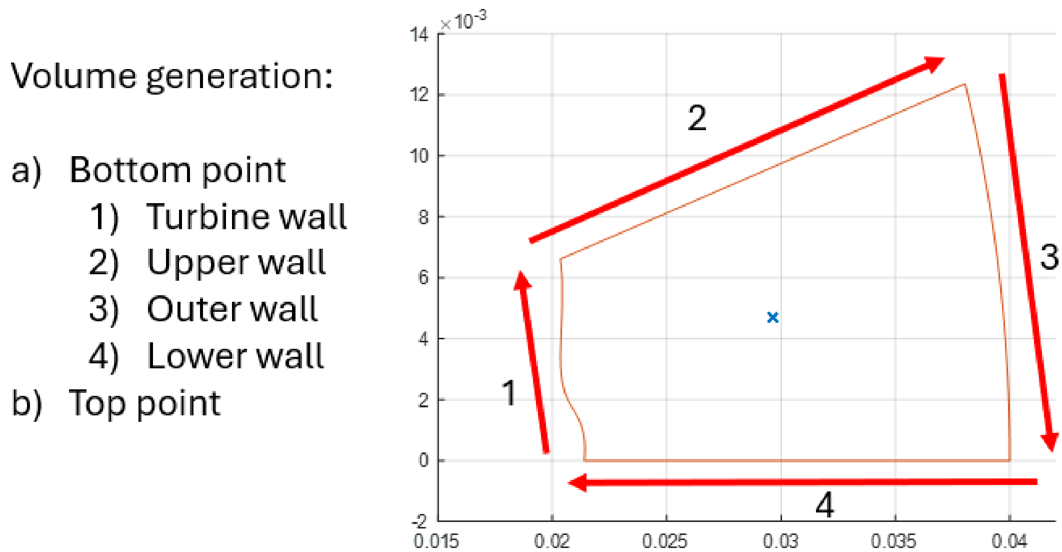

Figure 37. Domain generation technique in MATLAB.

The resulting fluid domain is shown below. This geometry is again exported as an .stl file, and was imported to HEXPRESS for mesh generation.

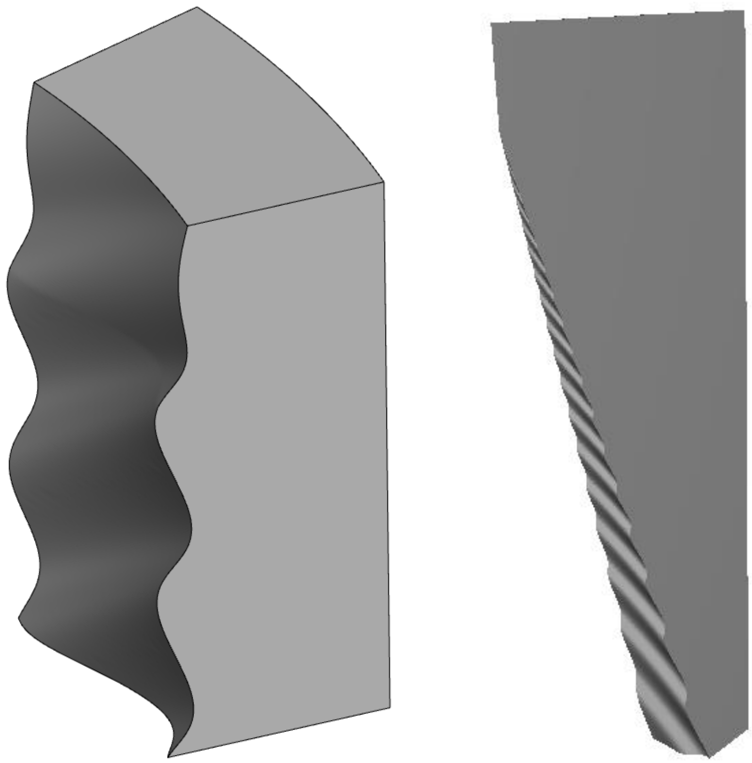

Figure 38. Completed air domains ready to be meshed. Left: Cylindrical, Right: Conical.

3.4.2 Mesh Generation

As previously mentioned, Numeca HEXPRESS was used to generate the mesh used for the CFD simulations. To more accurately capture the surface geometry of the turbines, global and surface refinement was enabled. By enabling this setting, the software aims to reduce the cell size in the specified regions to match the user's specifications.

Following the initial mesh generation, a viscous refinement layer was added to more accurately capture the boundary layer which forms over the turbine's surface. Using the y^+parameter discussed previously, a first-layer cell thickness of 0.5 μm was used with 20 inflation cells.

Initially, a cylindrical mesh was used for the CFD simulations. The refinement of the cylindrical mesh led to large gradients in cell density, creating discontinuities in fluid properties including pressure and temperature. For this reason, a rectangular mesh was instead used, using global surface refinement parameters to ensure mesh density gradients were not present along the surface of the turbine.

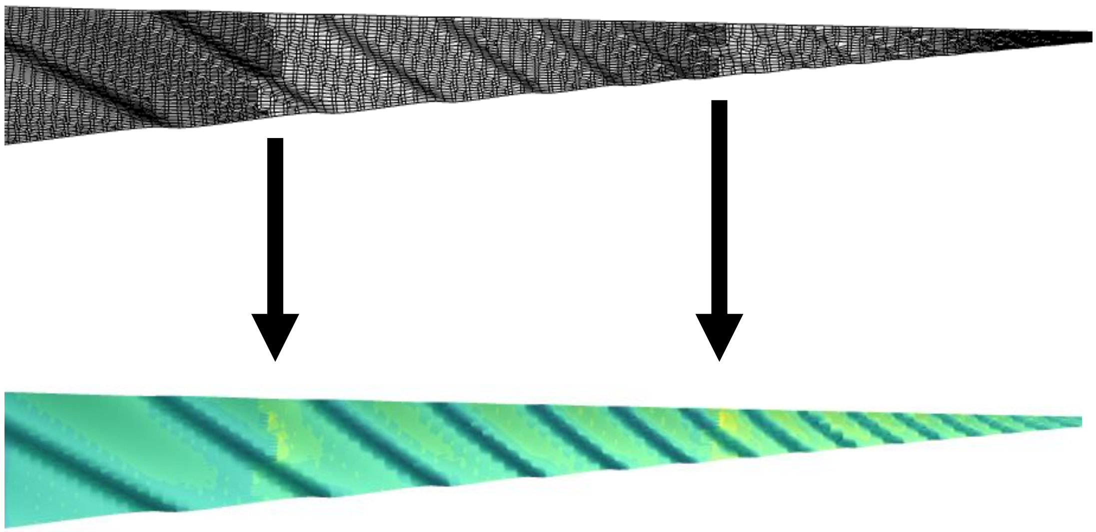

Figure 39. Discontinuity in mesh density leading to pressure gradients on turbine surface.

After completing a mesh sensitivity study, discussed further in later sections, the following settings were used for all future simulations. The final cell count was approximately 4.9 million.

Table 8. Mesh parameters used for conical bladeless turbine.

Initial mesh size	180 x 90 x 180
Refinement diffusion	4
Number of cells in gap	10
Minimum cell size	0
Maximum cell size	$1 \cdot 10^{20}$
Surface refinement	Enabled for turbine surface
First layer thickness	0.5 μm
Inflation layers	20

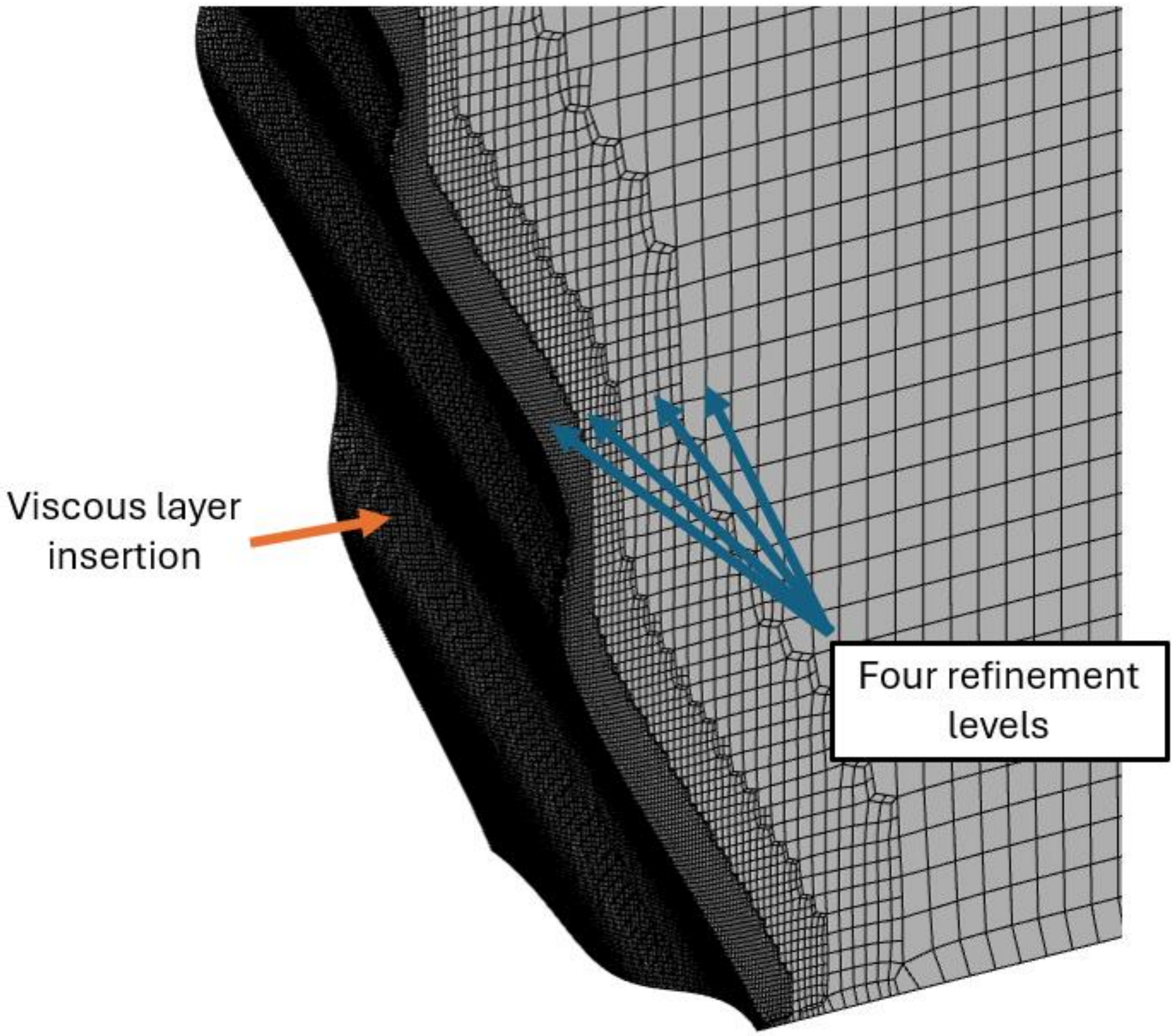

Figure 40. Completed mesh of conical bladeless turbine showing refinement levels and viscous layer.

3.4.3 CFD Simulations

Metacomp's iCFD++ was used for configuring and solving the computational cases. Steady-state RANS simulation was used for the solution type due to the time-invariant nature of the inlet flow. Air, modeled as a perfect gas, was used as the working fluid. For the turbulence model, a two equation $\kappa - \omega$ SST model was used for reasons discussed previously.

To simulate the rotational velocity of the turbine, mesh motion was specified to the CFD solver, with a specified rotational velocity equal to the rotational velocity of the turbine. As a result of this, the wavy surface of the turbine was specified as a viscous wall, stationary with respect to the mesh motion.

The angled walls of the fluid domain were specified as periodic boundary conditions with flow-through conditions. This effectively simulates the entire turbine while only requiring $\frac{1}{20}^{\text{th}}$ of the computational time for the same level of accuracy.

The inlet of the turbine's air domain was set as a supersonic inlet with $P_s = 150$ kPa, $T_s = 2300$ K, and $V = 1538\,\frac{\text{m}}{\text{s}}$, resulting in an inlet Mach number of 1.6. These conditions were chosen to correspond to the conditions used by Braun et. al., where the turbine would be placed downstream of a RDC [15]. The outlet conditions were specified as supersonic outflow.

After being configured, the CFD simulations were run on the NCSU Hazel High-Performance Computing cluster using 32 cores. Each simulation was completed in approximately three hours.

3.5 CFD Results

3.5.1 Convergence Criteria

To define convergence, a simulation was run for 2000 iterations, with the mass, energy and momentum residuals plotted below.

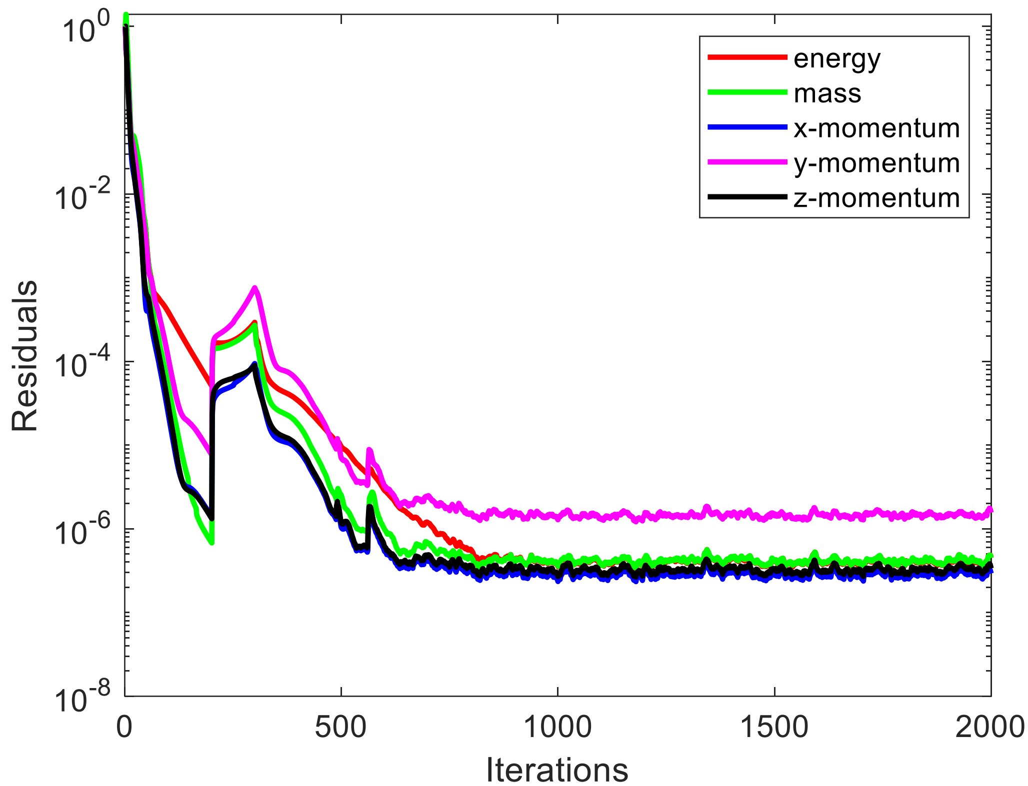

Figure 41. Plot of residuals for conical bladeless turbine CFD case.

The value of most interest for the characterization of the bladeless turbine is the torque production. As such, the torque acting on the turbine segment was calculated at each iteration, and is plotted below.

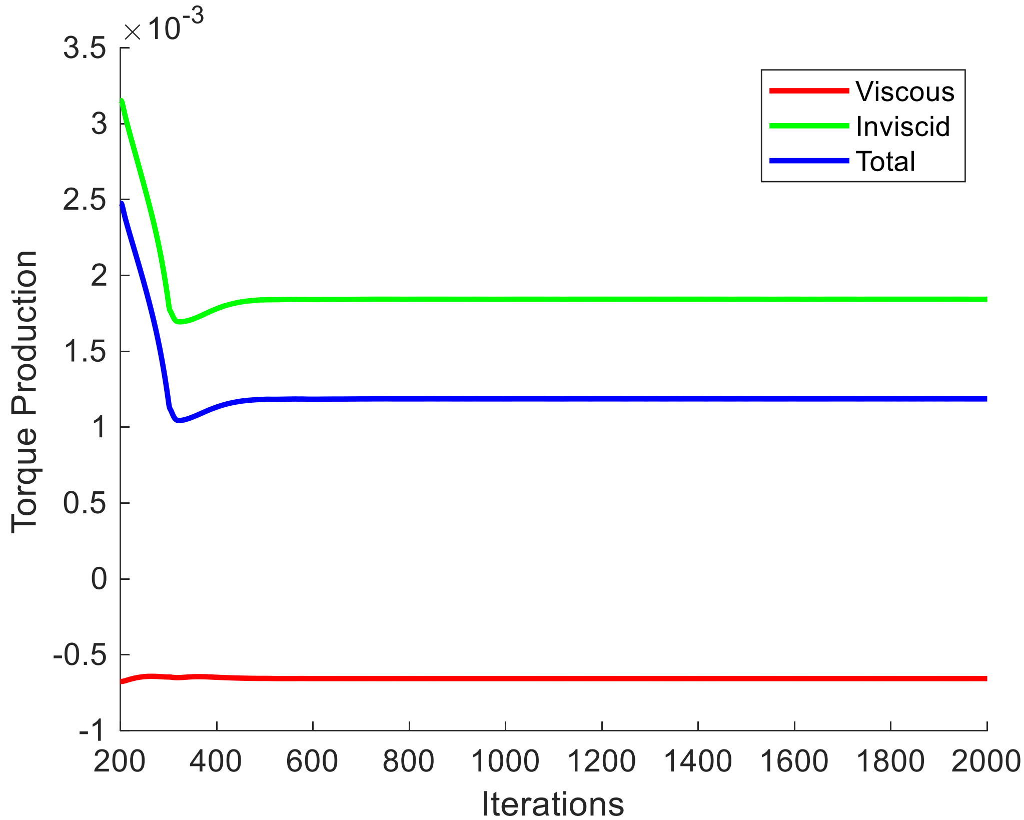

Figure 42. Plot of viscous, inviscid, and total torque production from iteration 200 to 2000.

As can be seen, there is little variation in torque production past iteration 600. Thus, iteration 750 was chosen as the convergence point, and all simulations were run for this duration.

3.5.2 Mesh Sensitivity

While meshes with higher cell counts can lead to simulation results with greater accuracy, a mesh with excessive cell count will not produce significant improvement in accuracy, while greatly increasing computational time. Studying the trade-off between cell count and simulation results is the purpose of a mesh refinement study. Such a study was performed on the conical bladeless turbine to determine the optimal cell count.

As previously mentioned, the performance parameter of greatest interest is the torque production of the turbine. Meshes ranging from 1.6 million to 6.2 million cells were generated and simulated, with the turbine's torque being plotted as a function of the cell count in the figure below, with the horizontal dotted lines representing $\pm 2\%$ of the torque produced by the 6.2 million cell mesh.

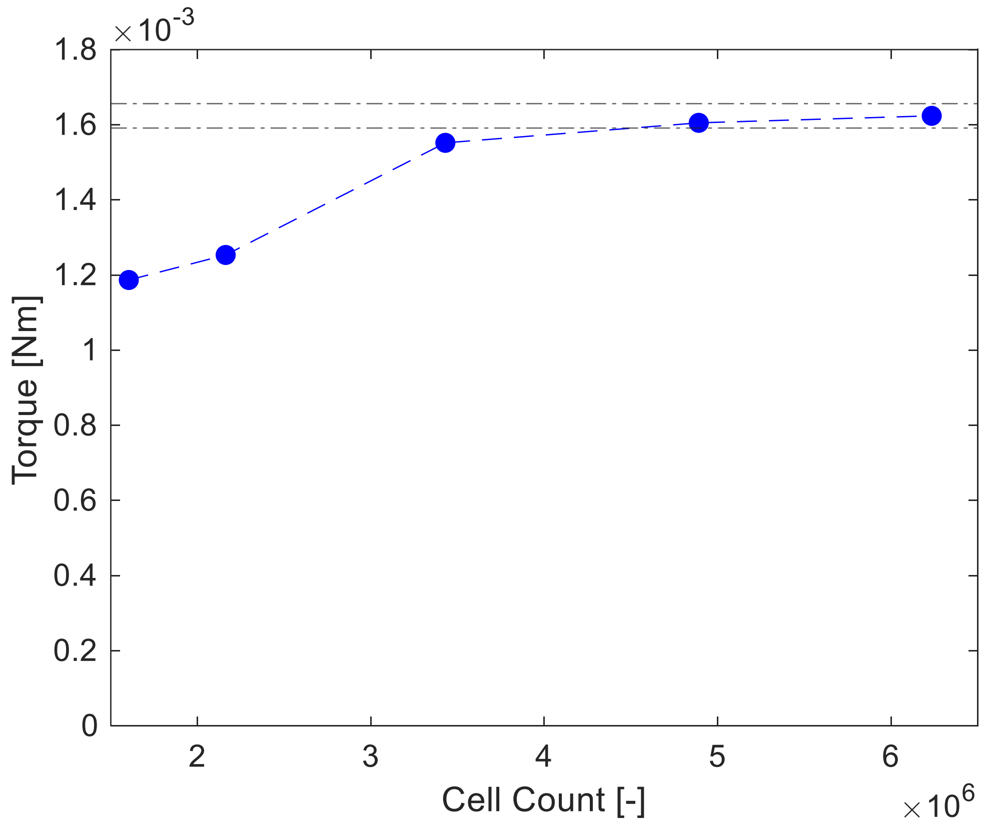

Figure 43. Conical bladeless turbine mesh refinement study results.

As can be seen, the torque of the turbine converges to the true value as the cell count increases. After completing the mesh refinement study, a cell count of approximately 5 million was selected for use in all future simulations.

3.5.3 Torque and Power Production

The goals of the computational simulations were to produce a plot of torque and power vs rotational rate for the conical bladeless turbine, and study the effect of wave amplitude on the power production. Similar to what was done in the sizing study, where the power output was predicted as a function of turbine diameter, variations in the inlet stagnation pressure and temperature were used to predict the power output. These variations in inlet conditions including pressure, temperature and Mach number were also simulated, with the results correlating well with the non-dimensional study.

Three different wave amplitudes were chosen to observe their effect on the torque and power production of the conical bladeless turbine. A linear relationship between torque production and rotational velocity was found, with the coefficients of determination being shown in the following table. Below are figures of the torque and power as functions of turbine rotational velocity.

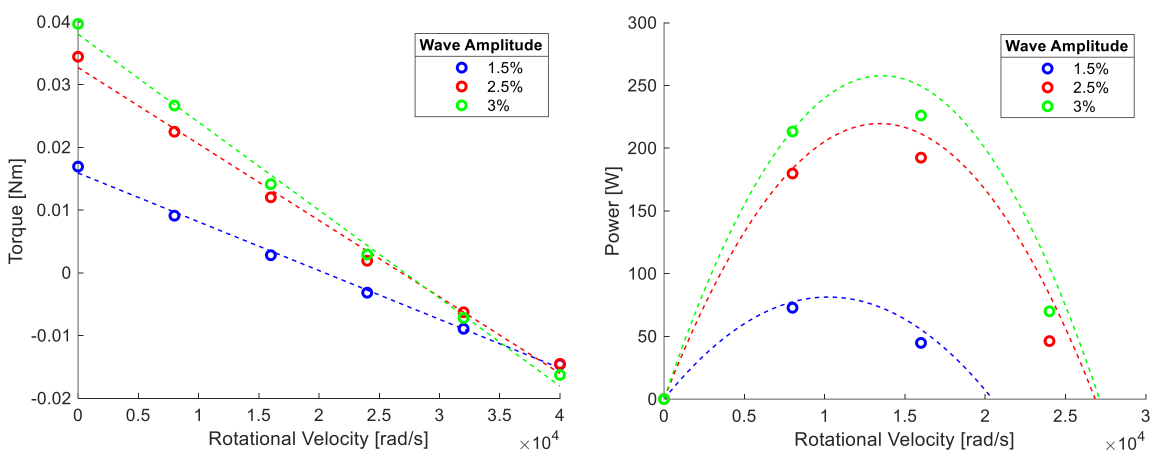

Figure 44. Plots of torque and power production of conical bladeless turbine.

Table 9. Coefficients of determination for linear torque vs rotational velocity curves

Wave Amplitude	1.5%	2.5%	3%
Linear fit torque vs RPM	0.9965	0.9944	0.9954

The conical bladeless turbines were able to produce over $200\,\mathrm{W}$ of mechanical output power at a rotational rate of $16000\,\frac{\mathrm{rad}}{\mathrm{s}}$. The high rotational rates chosen for the analysis come as a result of the small turbine diameter of 3 cm. The Mach number at the tip of the turbine remained very low, only reaching $\mathrm{Ma} = 0.13$. Many conventional turbomachines operate with tip speeds in the transonic regime, however with the small diameter of the turbine, the rotational velocity would be greater than what is practically possible in a laboratory environment. Additionally, the torque exhibited a linear behavior, dropping below zero above $24000\,\frac{\mathrm{rad}}{\mathrm{s}}$, making testing at higher rotational rates unnecessary.

Viscous and inviscid torque contributions were also plotted for the 3% amplitude case, with the results being shown below in a plot. Similar plots were obtained for the 1.5% and 2.5% case, with the primary difference being the reduction in the inviscid, and total torque production. The viscous contribution did not show significant variation with wave amplitude. As the rotational velocity of the turbines increase, the inviscid torque production decreases and is unable to overcome the viscous torque acting in the opposing direction. This leads to an overall reduction in torque output, which eventually reaches zero and becomes negative.

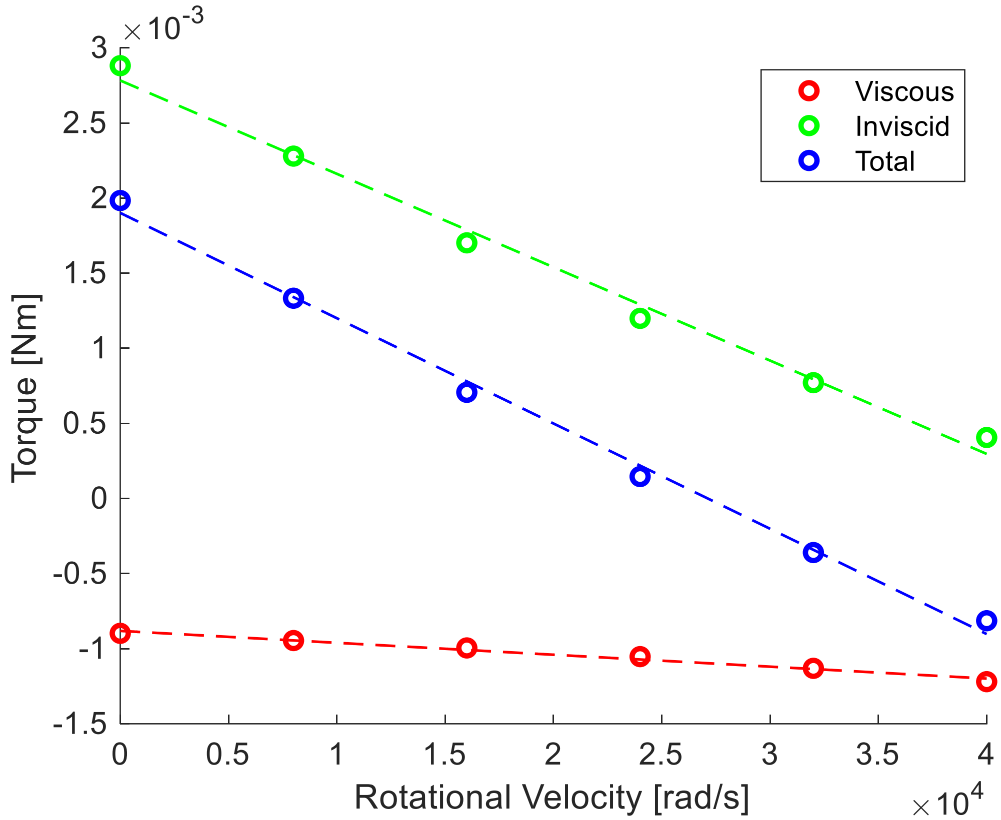

Figure 45. 3% amplitude conical bladeless turbine viscous, inviscid, and total torque production.

3.5.4 Contours of Fluid Properties

To visualize the presence of shockwaves and ensure the correct operation of the bladeless turbines, contours of Mach number and pressure are shown below. The results demonstrate the expected behavior, with strong pressure gradients occurring over the wavy surface, and an oblique shock wave at the front. Periodic fluctuations in the Mach number are visible at the surface of the waves, demonstrating the presence of expansion fans.

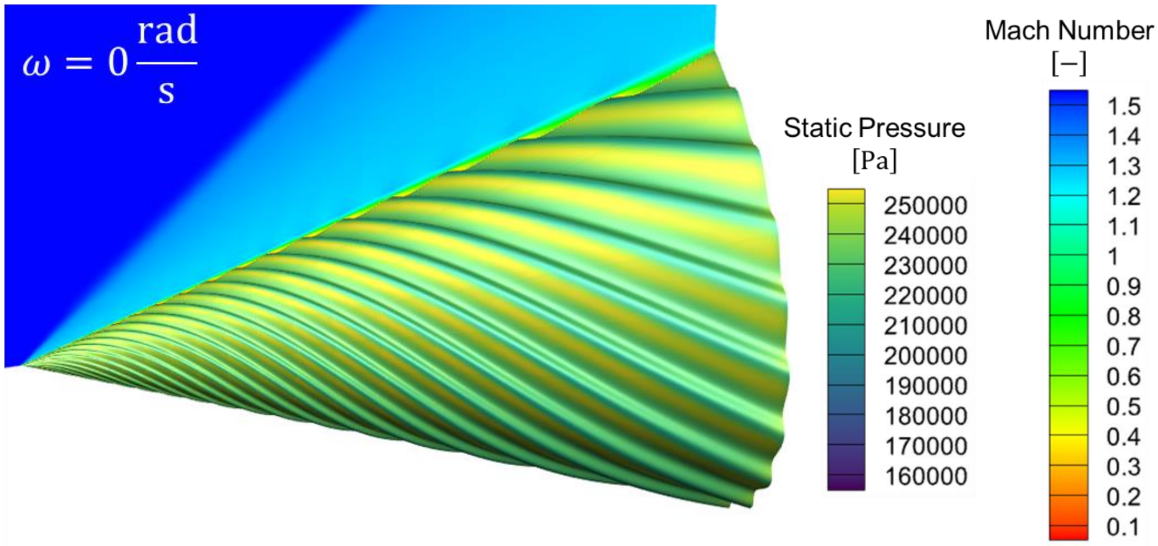

Figure 46. Plot of surface pressure and Mach number along axial direction of the conical bladeless turbine.

When comparing the plots of surface pressure to that of the turbine in motion, it is evident that the pressure differential across the surface of the waves is reduced. This results in a reduced torque production, which is also demonstrated in the plots of torque as a function of rotational rate presented above.

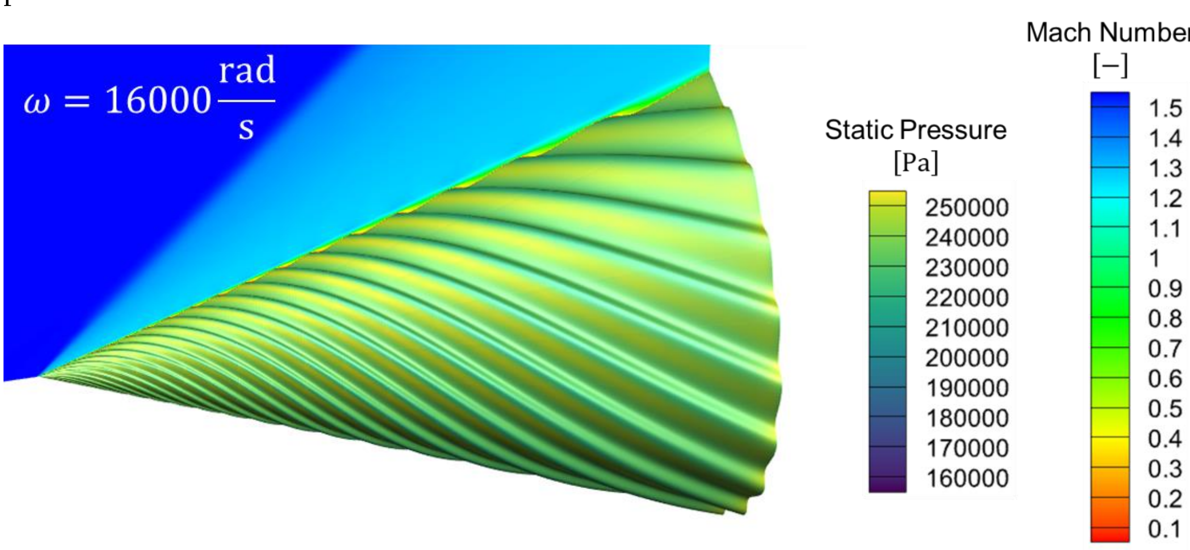

Figure 47. Plot of surface pressure and Mach number of rotating turbine, demonstrating reduced pressure differential.

4 Conclusions

4.1 Air Jet Spinning

In the air jet spinning study, three models were developed to predict the velocities of wrap fibers, providing a direct connection between the air flow field and the yarn production rate. The first model used the geometric features of the completed yarn, with the second and third models using results from CFD simulations to calculate the torque acting on a simplified wrap fiber due to aerodynamic drag. These models were applied to a Savio Lybra® air jet spinner to study the angular velocities of the wrap fibers during production. The geometric model predicted a velocity of approximately $26600\,\frac{\mathrm{rad}}{\mathrm{s}}$, while the first dynamic model predicted $28500\,\frac{\mathrm{rad}}{\mathrm{s}}$, and the second $30900\,\frac{\mathrm{rad}}{\mathrm{s}}$. These estimates lie within ranges suggested by existing literature, and serve as a way to quantify the performance of different spinning chamber and nozzle geometries.

In total, three sensitivity analyses were performed on the dynamic wrap fiber models, aiming to investigate the influence of input parameters on the wrap fiber's velocity. The first sensitivity study investigated the impact of the height of the wrap plane. In general, both the one-dimensional and two-dimensional models predicted a reduction in velocity as the wrap plane height increases. Next, the drag coefficient of the fiber was analyzed. The drag coefficient was found not to effect the one-dimensional model, but had a small effect on the two-dimensional model in the transient acceleration stage. Larger drag coefficients were able to accelerate the fiber more quickly, while the steady-state speed was mostly unaffected. Finally, various initial conditions were tested with the two-dimensional model. The initial angle and velocity of the wrap fibers did not have significant effects on the final steady-state velocity, with the exception of angles between $120°$ and $180°$. At these angles, the negative tangential air velocity in the spinning chamber resulted in a stationary equilibrium where the wrap fibers settled at $158°$ with zero velocity.

To validate the results of the proposed models with experimentation, modifications were made to a Savio Lybra® spinning chamber to enable optical access. Various designs were tested, with the final prototype using a curved quartz window. High speed imaging was taken using a FASTCAM NOVA high speed camera, and various macro lenses to achieve the desired magnification. Framerates up to 40000 FPS were used to capture the spinning process. The main challenge faced during the experimental measurements was adequate lighting due to the small imaging area, short exposure times, and high temporal resolution requirement. Despite these challenges, the results of the models showed strong correlation with experimental measurements, which suggested a velocity of approximately $28000\,\frac{\text{rad}}{\text{s}}$. Consequences of the rotational motion of the wrap fibers include a non-uniform tensile stress distribution, suggesting a maximum theoretical yarn production rate. These findings contribute to the understanding of air jet spinning and can serve as a basis for more complex models aiming to optimize the yarn production process.

4.2 Bladeless Turbine

The investigation of the bladeless turbine focused on modifications necessary for successful experimental testing. A non-dimensional sizing study was successfully performed, using the Buckingham-Pi theorem and similitude to reveal how the turbine's rotational rate and power production vary as a function of the turbine's diameter. The results of this study can also be used to study the effects of the inlet properties, including total pressure and temperature on parameters of interest.

A novel conical geometry was created to facilitate experimental testing in a uniform, axisymmetric flow field found at the exit of a converging-diverging nozzle. The conical geometry eliminates the need for an annular flow field, allowing the turbine to be tested in more conventional facilities. The results of the non-dimensional study were used to dictate the size of the conical turbine, with three wave amplitudes being simulated to investigate their effect on the turbine's power generation. Larger wave amplitudes were found to generate more power.

CFD simulations of the turbine were used to validate the hypothesized operational principal, with the results confirming the presence of shockwaves, expansion fans, and large pressure gradients. With a stationary turbine, a maximum pressure differential of 30 kPa was noted across the crest and trough of the turbine, while the rotating turbine experienced a pressure differential of 12 kPa. This trend led to the reduction in torque as the turbine velocity increased, eventually leading to zero torque production as the viscous losses began to dominate.

The performance analysis of the conical turbine demonstrated the potential advantages and limitations of bladeless power extractions, while the proposed modifications offer pathways for future experimental validation. A final design 3 cm in diameter with 3% wave amplitude demonstrated a power extraction of approximately 200 W. The size and shape of the turbine was specifically developed for implementation in a laboratory environment, suitable for testing in both cold flow and hot flow environments.

References

[1] F. White, *Fluid Mechanics*, 7th ed. New York: McGraw-Hill, 2009.

[2] M. Eldessouki, S. Ibrahim, and R. Farag, "Dynamic properties of air-jet yarns compared to rotor spinning," *Textile Research Journal*, vol. 85, no. 17, pp. 1827–1837, 2015, doi: 10.1177/0040517514563726.

[3] G. Karakan Günaydin and A. Serkan Soydan, "Vortex Spinning System and Vortex Yarn Structure," 2016, doi: 10.5772/105882.

[4] M. R. A. Bhatti, M. Tausif, M. A. Mir, M. Umar, and T. Cassidy, "Effect of key process variables on mechanical properties of blended vortex spun yarns," *Journal of the Textile Institute*, vol. 110, no. 6, pp. 932–940, Jun. 2019, doi: 10.1080/00405000.2018.1532784.

[5] J. Braun, G. Paniagua, F. Falempin, and B. Le Naour, "Design and Experimental Assessment of Bladeless Turbines for Axial Inlet Supersonic Flows," *J Eng Gas Turbine Power*, vol. 142, no. 4, Apr. 2020, doi: 10.1115/1.4045359.

[6] M. Eldeeb and E. Moučková, "Numerical simulation of the yarn formation process in Rieter air jet spinning," *Journal of the Textile Institute*, vol. 108, no. 7, pp. 1219–1226, Jul. 2017, doi: 10.1080/00405000.2016.1230000.

[7] H. Guo, X. An, and C. Yu, "Numerical Study on the Principle of Yarn Formation in Murata Air-Jet Spinning," 2007.

[8] Y. C. Zeng and C. W. Yu, "Numerical Simulation of Fiber Motion in the Nozzle of an Air-Jet Spinning Machine."

[9] A. Osman, B. Malengier, S. De Meulemeester, J. Peeters, J. Vierendeels, and J. Degroote, "Simulation of air flow–yarn interaction inside the main nozzle of an air jet loom," May 01, 2018, *SAGE Publications Ltd*. doi: 10.1177/0040517517697646.

[10] C. Han, L. Cheng, W. Gao, Y. Xue, W. Xue, and R. Yang, "Numerical simulation and analysis of the dynamic finite element model of the fiber motion in the air spinning process," *Textile Research Journal*, vol. 89, no. 7, pp. 1198–1206, Apr. 2019, doi: 10.1177/0040517518764023.

[11] S. Kacker and U. Okapuu, "A Mean Line Prediction Method for Axial Flow Turbine Efficiency," Jan. 1982. [Online]. Available: http://asmedigitalcollection.asme.org/gasturbinespower/article-pdf/104/1/111/5529077/111_1.pdf

[12] J. Mee, N. C. Baines, G. Oldfield, and T. E. Dickens, "An Examination of the Contributions to Loss on a Transonic Turbine Blade in Cascade," 1992. [Online]. Available: http://asmedigitalcollection.asme.org/turbomachinery/article-pdf/114/1/155/5604398/155_1.pdf

[13] A. Grönman, T. Turunen-Saaresti, A. Jaatinen, and J. Backman, "Numerical modelling of a supersonic axial turbine stator," *Journal of Thermal Science*, vol. 19, no. 3, pp. 211–217, Sep. 2010, doi: 10.1007/s11630-010-0211-5.

[14] A. M. K. Abdalhamid and A. Eltaweel, "Design and analysis of a single-stage supersonic turbine with partial admission," *Energy*, vol. 309, Nov. 2024, doi: 10.1016/j.energy.2024.133100.

[15] J. Braun, G. Paniagua, and F. Falempin, "Aerothermal optimization of bladeless turbines," *J Eng Gas Turbine Power*, vol. 143, no. 3, Mar. 2021, doi: 10.1115/1.4049355.

[16] J. Braun, F. Falempin, and G. Paniagua, “Energy analysis of a detonation combustor with a bladeless turbine, a propulsion unit for subsonic to hypersonic flight,” *Energy Convers Manag*, vol. 262, Jun. 2022, doi: 10.1016/j.enconman.2022.115491.
[17] Y. C. Zeng and C. W. Yu, “Numerical Simulation of Air Flow in the Nozzle of an Air-Jet Spinning Machine 1,” 2003.
[18] Z. Zou, S. Zheng, L. Cheng, B. Xi, and J. Yao, “Effect of Some Variables on the Fibre Packing Pattern in a Yarn Cross-section for Vortex Spun Yarn,” 2014.
[19] A. Kyaw Soe, M. Takahashi, M. Nakajima, and T. Matsumoto, “Structure and Properties of MVS Yarns in Comparison with Ring Yarns and Open-End Rotor Spun Yarns.”
[20] R. A. Angelova, “Air-jet spinning,” *Advances in Yarn Spinning Technology*, pp. 315–344, Jan. 2010, doi: 10.1533/9780857090218.2.315.
[21] M. Eldeeb, “DIFFERENT APPROACHES FOR PREDICTING AIR JET SPUN YARN STRENGTH,” Liberec, 2017.
[22] D. Kremenakova, “VORTEX YARN STRUCTURE CHARACTERIZATION,” Liberec, Jan. 2013. [Online]. Available: http://www.muratec-vortex.com.
[23] G. Basal, “The Structure and Properties of Vortex and Compact Spun Yarns,” 2003.
[24] Z. Zou, J. yu, W. Xue, Y. Zhu, J. wu, and L. Cheng, “Analysis of the Fiber Spatial Trajectory in Vortex Spun Yarn,” *Textile Research Journal*, vol. 79, no. 10, pp. 924–929, 2009, doi: 10.1177/0040517508095609.
[25] A. Basu, “Progress in air-jet spinning,” *Progress in Air-Jet Spinning*, p. 1, 1999, doi: 10.1080/00405169908688877.
[26] Z. Zou, L. Cheng, B. xi, Y. Luo, and Y. Liu, “Investigation of fiber trajectory affected by some parameter variables in vortex spun yarn,” *Textile Research Journal*, vol. 85, no. 2, pp. 180–187, 2015, doi: 10.1177/0040517513509873.
[27] ANSYS, “What is Computational Fluid Dynamics (CFD)?” Accessed: Mar. 01, 2025. [Online]. Available: https://www.ansys.com/simulation-topics/what-is-computational-fluid-dynamics
[28] T. V. B. Phung, A. Yoshida, Y. Iemoto, H. Uematsu, and S. Tanoue, “Numerical simulation of airflow characteristics in the spinning zone at starting time of air-jet spinning machine,” *Textile Research Journal*, vol. 89, no. 12, pp. 2342–2352, Jun. 2019, doi: 10.1177/0040517518792743.
[29] S. Chakravarthy, O. Peroomian, U. Goldberg, and S. Palaniswamy, “The CFD++ Computational Fluid Dynamics Software Suite,” 2025.
[30] Z. Pei and C. Yu, “Study on the Principle of Yarn Formation of Murata Vortex Spinning Using Numerical Simulation,” *Textile Research Journal*, vol. 79, no. 14, pp. 1274–1280, 2009, doi: 10.1177/0040517509102227.
[31] Y. C. Zeng, J. P. Yang, and C. W. Yu, “Mixed Euler-Lagrange approach to modeling fiber motion in high speed air flow,” *Appl Math Model*, vol. 29, no. 3, pp. 253–261, Mar. 2005, doi: 10.1016/j.apm.2004.09.007.
[32] R. K. Finn, “Determination of the drag on a cylinder at low Reynolds numbers,” *J Appl Phys*, vol. 24, no. 6, pp. 771–773, 1953, doi: 10.1063/1.1721373.
[33] C. Wieselsberger, “New Data on the Laws of Fluid Resistance,” *Physikalische Zetischrift*, no. 22, pp. 321–328, 1921.
[34] D. A. Potts, “Hydrodynamics of Vertical Surface-Piercing Cylinders,” University of Tasmania, 2019. [Online]. Available: https://www.researchgate.net/publication/338720559

[35] H. W. Krause, “STAPLE-FIBRE SPINNING SYSTEMS.,” *Journal of the Textile Institute*, vol. 76, no. 3, pp. 185–195, 1985, doi: 10.1080/00405008508658500.
[36] T. Nakahara, “Air-Jet Spinning Technology,” *Text. Technol. Intl.*, pp. 73–74, 1988.
[37] L. Talluri, D. Fiaschi, G. Neri, and L. Ciappi, “Design and optimization of a Tesla turbine for ORC applications,” *Appl Energy*, vol. 226, pp. 300–319, Sep. 2018, doi: 10.1016/J.APENERGY.2018.05.057.
[38] A. L. Neckel and M. Godinho, “Influence of geometry on the efficiency of convergent–divergent nozzles applied to Tesla turbines,” *Exp Therm Fluid Sci*, vol. 62, pp. 131–140, Apr. 2015, doi: 10.1016/J.EXPTHERMFLUSCI.2014.12.007.
[39] N. Vinha, G. Paniagua, J. Sousa, and B. H. Saracoglu, “Axial bladeless turbine suitable for high supersonic flows,” *J Propuls Power*, vol. 32, no. 4, pp. 975–983, 2016, doi: 10.2514/1.B35818.
[40] W. B. Foor and W. Jansen, “THE APPLICATION OF AIR DYNAMOMETERS FOR TESTING TURBO-SHAFT GAS TURBINE ENGINES,” 1984. [Online]. Available: http://asmedigitalcollection.asme.org/GT/proceedings-pdf/GT1984/79467/V001T01A059/2395454/v001t01a059-84-gt-216.pdf
[41] S. Sasaki, “A High-Speed Dynamometer Developed to Measure a Small Gas Turbine Engine’s Output,” *SAE Technical Paper Series*, Mar. 1983.
[42] Z. Yang, “Gas Turbine Dynamic Dynamometry: A New Energy Engineering Laboratory Module,” Milwaukee, Oct. 2013. doi: 10.18260/1-2-1115-36218.
[43] S. A. Sjolander, “MECH 4305A FLUID MACHINERY SUPPLEMENTARY COURSE NOTES,” Ottawa, 2022.
[44] G. Lohsen, “stlwrite - Write binary or ascii STL file.” Accessed: Mar. 01, 2025. [Online]. Available: Grant Lohsen (2025). stlwrite - Write binary or ascii STL file (https://www.mathworks.com/matlabcentral/fileexchange/36770-stlwrite-write-binary-or-ascii-stl-file), MATLAB Central File Exchange. Retrieved March 2, 2025.